Antenna design of a radar phased array using drone swarms

Hanna Norrud
hanna.norrud@gmail.com

Department of Electrical and Information Technology
Lund University

Supervisor: Daniel Sjöberg

Examiner: Erik Lind

January 20, 2025

Printed in Sweden
Tryckeriet i E-huset, Lund

Abstract

A distributed phased array allows full position freedom of the individual radar system nodes, still resulting in corporative and cohesive measurements. Recent and ongoing advancements in synchronization between the radar system nodes make the implementation of such a system increasingly feasible. To fully exploit the freedom of node placement, the use of drones as system carriers is investigated. The use of drones offer efficient maneuvering, enabling fast position adjustments and increases access to areas typically hard to reach. However, implementing such a system is not without challenges. These include insuring coherence between the system nodes as well as integrating the system at the drone with limited space and load capacity. In this thesis, antennas are proposed to be installed on the drone. The result is based on simulations, and include a modeled drone along with the antenna, feed and mounting arrangements. One of the proposed designs, the half-wavelength dipole antenna, yields a lightweight solution with desired radiation properties for a potential radar application. This design supports a distributed phased array forming a common wavefront.

Keywords: Distributed Phased Array, Drone, Antenna Design, Radar, SDR

Declaration

I hereby affirm that this Master thesis was composed by myself, that the work herein is my own except where explicitly stated otherwise in the text. This work has not been submitted for any other degree or professional qualification except as specified; nor has it been published. Where other people's work has been used (either from a printed source, internet, or any other source), this has been carefully acknowledged and referenced.

AI, specifically Writefull and ChatGPT-4 has provided assistance throughout the execution of the thesis. It has been used by clarifying confusions, getting second opinions on approximations and making smaller refinements on figures. Additionally, it has been used to improve the text, checking for spelling and grammatical errors.

Acknowledgements

To start, I would like to express my gratitude to my supervisor Daniel Sjöberg, whose enthusiasm initially inspired me towards the subject. Throughout the project, he has been a constant source of guidance and has always found the time to share knowledge, discuss ideas and sort out any confusions. Secondly, I want to thank WARA-PS for sharing detailed information on the hardware of the drone used in the project, which allowed for more accurate results. Finally, I want to thank my family for their encouragement and support.

Popular Science Summary

Picture a classic green radar screen with a sweeping beam that illuminated targets as it rotates. This image has long been associated with radar, but also ties directly to one of the most iconic and early uses of radar systems, i.e., search and detect. Originally designed to mechanically scan a volume of space and detect objects, such as aircrafts, by measuring their distance and velocity, this radar application has been vital for decades. Even today, this role remains one of the most significant radar applications. However, at its core, a radar system is simply a sensor, a tool that measures range and velocity. Its true potential lies in how creatively we apply it, driven by innovative ideas and solutions.

When it comes to sensors, whether to explain a concept or draw inspiration for new innovative ideas, it has proven helpful to look at one of the ultimate designers: nature. Systems in nature have been optimized by evolution over hundreds of thousands of years and offer great examples of both deceptively simple and quite complex solutions. Take, for example, the security system of the meerkats. These small mammals have developed a highly effective way to monitor their surroundings. Meerkats take turns standing guard on elevated spots like hills, either in a fixed location or spread out across different points near their home. When they suspect or detect a threat, they communicate with one another in a coordinated response.

A phased distributed radar array has embraced similar principles and addresses the two concepts discussed so far. First, unlike traditional systems, it can steer a beam without requiring a mechanically rotating platform. Instead, it uses the signal properties of individual sensors, which work together to create a coordinated final signal. Second, much like the meerkats, each radar sensor in such a system operates independently but collaborates to form a comprehensive picture and make decisions about the scene. The key term here is *coordination*, ensuring that the sensors function as one. Synchronizing multiple radar systems to cooperate effectively is a rapidly advancing field of research.

The focus of this thesis is to evaluate such a distributed radar system, with each radar implemented on a drone. This introduces additional challenges, including the limited space and weight that can be carried, as well as the limited mission time imposed by the drone platform. The primary goal of the project is to design an antenna, the unit responsible for transmitting and receiving the signal, that is tailored to meet these demands, while allowing drones to function as a cohesive and efficient radar array.

The radar phased array, which creates a coordinated final signal, was chosen as the application because it does not require the individual radar sensors to be steered. To achieve this, antennas must exhibit broad radiation patterns to ensure overlapping illumination, allowing signals from all units to combine effectively.

Three antenna types with broad radiation were investigated: the half-wavelength dipole antenna, the monopole antenna, and a characteristic mode antenna, where the drone itself functions as an antenna. Among these, the half-wavelength dipole antenna proved to be the most adaptable, as it delivered desired radiation properties when placed at various places around the drone. In addition, it remained lightweight and fully compatible with other components of the system, such as the unit that delivers the signal.

Table of Contents

Abbreviations

CCE Capacitive Coupling Element

CM Characteristic Mode

CPI Coherent Processing Interval

CW Continuous Wave

EM Electromagnetic

FPGA Field-Programmable Gate Array

HPBW Half-power Beam Width

ICE Inductive Coupling Element

MS Modal Significance

MW Modal Weight

PEC Perfect Electrical Conductor

PRF Pulse Repetition Frequency

PRI Pulse Repetition Interval

RF Radio Frequency

SAR Synthetic Radar Aperture

SBC Single-Board Computer

SDR Software Defined Radio

UAV Unmanned Aerial Vehicles

Rx Receiver

Tx Transmitter

Chapter 1

Introduction

1.1 Background

In recent decades, natural disasters have occurred more frequently than previously recorded [1]. Events such as wildfires and earthquakes often demand rapid response in environments with limited accessibility and visibility. At the same time, global conflicts have evolved with the integration of advanced technologies. For example, in November 2024, the Armed Conflict Location & Event Data (ACLED) recorded over 10 000 drone or airborne attacks [2], demonstrating the growing role of unmanned systems in various domains. While this example highlights the use of drones in warfare, their potential extend far beyond.

The potential of unmanned aerial vehicles (UAVs), or drones, has resulted in the rapid advancement of software for high-precision drone control and path planning [3]. Radar systems, which were initially constructed to measure only the range to a reflecting object, are now used in much more advanced ways, capable of detecting ranges, velocities, and even producing images. Given the UAVs' maneuverability and ability to reach most areas, drone-carried radar systems have naturally gained interest, and imaging and vital sign detection are two examples of their applications [4][5]. Current advancements include the use of multiple drones that work together for a single task, prompting developments in drone formation control and leading to the concept of drone swarms [6].

Phased arrays enable precise radiation control, allowing for both beamforming and beamsteering capabilities. Due to these properties, phased arrays are utilized in several radar applications, such as surveillance, remote sensing, and space exploration, and they remain a highly researched subject. However, the traditional half-wavelength spacing of antenna elements imposes limitations on such systems, particularly at low frequencies, where the resulting large size often makes the array stationary.

The advancement of drone swarms presents the possibility of realizing a highly controllable, mobile phased array radar, with each drone representing a single radar system. Such a system would be particularly useful when cameras are unsuitable, for example, when longer detection ranges are required or in obscured conditions, such as through rubble or smoke.

1.2 Goal

Implementing a drone carried phased array radar system presents several challenges, such as antenna design, challenges due to vibrations and position uncertainties of the drones, as well as communication and synchronization between the radar systems. In this project, the main goal is to design a lightweight antenna that is possible to carry on the DJI Matrice 100 quadcopter, without impairing its flying ability. The antenna must be well integrated with the remaining components of the radar system that will also be carried by the drone.

To ensure that the antenna is suitable for future applications, the project will begin by exploring possible radar systems based on available hardware. This approach will yield several design suggestions with varying levels of suitability. These designs will then be further evaluated, with potential challenges in antenna integration identified and solutions proposed. By addressing these challenges early, the integration process can be efficient and adaptable regardless of the specific final application.

1.3 Related Work

A key challenge in the implementation of the phased array radar system, which is distributed in space using drones, is the synchronization of phase and frequency between individual systems. Achieving this is essential for fully exploiting the benefits of phased arrays.

The authors in [7] achieved a time synchronization precision of 2.26 picoseconds between two stationary radar systems. This was accomplished by having each radar system adjust their clock and frequency to a common reference signal. The reference signal, generated by an external radio, consists of a two-tone signal that enables each radar system to measure the time delay and phase difference between the two tones and adjust its clock and frequency accordingly.

Rather than using an external reference, [8] demonstrates how the reference signal is exchanged directly between individual radar systems, enabling phase and frequency adjustments. This method enables synchronization among radar systems even while in motion. The results demonstrated precise synchronization and beamforming capabilities, approaching ideal performance.

In [9], a mathematical model of a phased array operating at 1 GHz and implemented on UAVs was investigated. The study demonstrated promising beamforming capabilities while exploring the effects of positional uncertainties and the number of antenna elements used. The results showed that employing a sufficient number of radar systems, even with moderate positional uncertainties, led to effective beamforming capabilities.

Chapter 2

Theory

The foundation of electromagnetism (EM) was established by James Clerk Maxwell in the 19th century, through his mathematical description of the physics of electromagnetism, summarized in four equations, known as Maxwell's equations [10]:

$$\nabla \times \boldsymbol{E} = -\mathrm{j}\omega \boldsymbol{B} \tag{2.1}$$
$$\nabla \times \boldsymbol{H} = \boldsymbol{J} + \mathrm{j}\omega \boldsymbol{D} \tag{2.2}$$
$$\nabla \cdot \boldsymbol{D} = \rho \tag{2.3}$$
$$\nabla \cdot \boldsymbol{B} = 0 \tag{2.4}$$

where they are given in the frequency domain assuming a time-harmonic field, and $\boldsymbol{E}$ and $\boldsymbol{H}$ are the electric and magnetic field strengths, $\boldsymbol{D}$ is the electric displacement, $\boldsymbol{B}$ is the magnetic flux density, $\boldsymbol{J}$ and ρ are the current and charge densities and ω is the angular velocity. The following convention between the time and phase domain is used:

$$\boldsymbol{E}(\boldsymbol{r}, t) = \mathrm{Re}\{\boldsymbol{E}(\boldsymbol{r}, \omega)\mathrm{e}^{\mathrm{j}\omega t}\} \tag{2.5}$$

Throughout this report, the analysis will be conducted in the frequency domain. When simplified as $\boldsymbol{E}$ or $\boldsymbol{E}(\boldsymbol{r})$, $\boldsymbol{E}(\boldsymbol{r}, \omega)$ is assumed.

When considering a homogeneous medium with linear properties in the absence of sources, Equations (2.1)-(2.4) can be re-written as:

$$\nabla^2 \boldsymbol{E} + \frac{\omega^2}{v^2}\boldsymbol{E} = 0$$
$$\nabla^2 \boldsymbol{B} + \frac{\omega^2}{v^2}\boldsymbol{B} = 0$$

where v is the propagation speed of the EM wave. The wave nature of the EM fields is one of many discoveries in the mathematical representation, and the EM wave is characterized by an amplitude and a phase that carry energy while propagating through space with a velocity. Basic wave characteristics, such as superposition, wave polarization and diffraction therefore appear significant in many EM applications. This also causes the parameters frequency f, wave number k, wavelength λ and angular velocity ω to be frequently used and the relationship between them is summarized as:

$$k = \frac{2\pi}{\lambda} \quad f = \frac{c}{\lambda} \quad \omega = 2\pi f$$

Moreover, the flux of power through a surface is described by the time-average of the Poynting vector [10]:

$$\langle \boldsymbol{S} \rangle = \frac{1}{2}\mathrm{Re}\{\boldsymbol{E} \times \boldsymbol{H}^*\} \tag{2.6}$$

Finally, for a plane wave, the following relationship holds:

$$\boldsymbol{B} = c^{-1}\hat{\boldsymbol{k}} \times \boldsymbol{E} \tag{2.7}$$

where c is the speed of light, and $\hat{\boldsymbol{k}}$ is the normalized wave vector, giving the direction of propagation of the wave. The following sections cover the theory of EM applications needed for the project. The first section addresses basic radar theory, followed by general antenna theory. Subsequently, a more detailed description of phased arrays and three types of antennas with particular importance is provided.

2.1 Radar System

A radar system uses the mentioned wave characteristics of the EM fields to determine either, or both, the position and the radial velocity of a potential target. By measuring the time ΔT between transmission and return of a reflected signal, the distance R can be calculated [11, p.4]:

$$R = \frac{c\Delta T}{2} \tag{2.8}$$

To determine the radial velocity of a target, v_r, the Doppler shift f_d, of the returned signal is measured [11, p.23]:

$$f_\mathrm{d} = \frac{2v_\mathrm{r}}{\lambda} \tag{2.9}$$

where λ is the wavelength of the signal. Regardless of the radar measurement, the returned signal must be strong enough for detection. The radar range equation considers the power loss of the full signal path and can be expressed as follows [11, p.73]:

$$\mathrm{SNR} = \frac{P_\mathrm{avg} T_\mathrm{d} G_\mathrm{r} G_\mathrm{t} \lambda^2 \sigma}{(4\pi)^3 R^4 k T_0 F L_\mathrm{s}} \tag{2.10}$$

Here SNR is the signal-to-noise ratio, P_avg is the average power, T_d is the Coherent Processing Interval (CPI), G_t and G_r are the gains of the transmitting and receiving antenna, λ is the wavelength, σ is the radar cross section of the target, R is the distance between radar system and target, k is the Boltzmann constant, T_0 is standard temperature (290 K), F is the noise figure and L_s is the total system loss.

There are many ways to utilize the EM waves characteristics to implement a radar system, and consequently a general description of a working system is challenging to give without in one way or another making a decision on the system. Therefore, it is helpful to consider broad categorizations of radar systems. A radar system can be characterized by which waveform is used, or by which one of the following applications it is to be used for; search, track, or imaging. The waveform and radar application type will be briefly explained in the following sections.

2.1.1 Radar waveform

The transmitted wave can be a pulsed wave or a continuous wave. A pulsed wave transmits for a given duration, giving the pulse width τ, followed by a listening time. During the listening time, before the next pulse is transmitted, there is a window of time in which a target reflection can be registered. The pulse width and the listening time add up to the Pulse Repetition Interval (PRI) or its inverse, the Pulse Repetition Frequency (PRF). The previously mentioned coherent processing interval is given by:

$$T_{\mathrm{d}} = n \cdot \mathrm{PRI} \tag{2.11}$$

where n is the number of pulses used.

Since the detection time is limited, the detection range is also restricted. In addition, when targets are close enough for the reflected signal to return within τ, the signal cannot be detected. However, the system is naturally divided in transmitting and receiving time, and therefore isolation between the two is usually effortless, and the same system is sometimes even used for both. The CW radar, on the other hand, continuously transmits a signal and the received signal is often many orders of magnitude smaller than the transmitted signal, requiring a sensitive receiver. Therefore, to prevent transmitter interference with the receiver, high isolation is required.

2.1.2 Search, track and imaging application

For search radar systems, it is essential to balance scan speed, detection probability, and false alarm minimization. The total scan time for a given volume depends on the angular coverage and the beamwidth in both the elevation and azimuth directions. Furthermore, the dwell time of the antenna, related to the angular scan rate, affects the scan time, and the use of a pulsed waveform introduces an additional factor based on the number of pulses and the duration of the pulse. This results in a trade-off between faster scanning speeds and reduced angular accuracy or coverage.

For effective target tracking, high-resolution signal processing is required. Range resolution is a key factor, as it determines how accurately the system can measure target distances. This resolution improves with an increase in signal bandwidth, but a higher bandwidth also introduces more noise, which lowers the signal-to-noise ratio (SNR) and limits the tracking range.

In radar imaging, Synthetic Aperture Radar (SAR) techniques help improve resolution by artificially increasing the antenna size through the platform's movement. Although range resolution remains important, cross-range resolution becomes significant. This is determined by the radar wavelength and the integration angle, which depend on the radar's movement and distance to the target scene. The trade-offs between range and cross-range resolution are important when designing and optimizing radar systems for both scanning and imaging applications.

2.2 Antenna Analysis

Radiation, or EM fields that transmit energy away from a source, is generated by accelerating charges. When designing an antenna, the shape of the currents along its structure is carefully considered to produce the desired radiation pattern. Calculating the exact fields from Maxwell's equations from a single accelerating particle is analytically challenging, and for an entire structure, it becomes impractical for a general understanding of antenna operation. Moreover, the radiated fields induce currents in nearby objects, making the antenna's environment a further complication in exact analytical calculations. Fortunately, effective approximations and analysis tools are available, and the most important ones will be discussed next.

2.2.1 Antenna radiation

Most of the parameters that quantify antenna radiation performance are defined in the so-called far-field region. The far-field is at a distance from the radiation source where the following holds [12]:

$$\boldsymbol{E}(\boldsymbol{r}) = \boldsymbol{E}(r,\theta,\phi) = \boldsymbol{F}(\theta,\phi)\frac{\mathrm{e}^{-\mathrm{j}kr}}{r} \tag{2.12}$$

This result is interpreted as the radiation pattern being independent of the radial distance, with the amplitude decreasing proportional to the distance. The accuracy of the far-field assumption increases with distance, but a common limit is typically defined as being at a distance of $2D^2/\lambda$ from the radiating element, where D is the largest dimension of the radiating element and λ is the wavelength of the radiation [12]. To evaluate the radiation, the radiation intensity $U(\hat{\boldsymbol{r}})$, is a measure of the power radiated per unit solid angle, and is obtained by scaling the average power density, i.e., the time-average of the Poynting vector in Equation (2.6), with the distance squared:

$$U(\hat{\boldsymbol{r}}) = U(\theta,\phi) = \frac{r^2}{2}\mathrm{Re}\{\boldsymbol{E}(\boldsymbol{r}) \times \boldsymbol{H}^*(\boldsymbol{r})\} = \frac{r^2}{2\eta}|\boldsymbol{E}(\boldsymbol{r})|^2 \tag{2.13}$$

where η is the wave impedance. Further, the total radiated power P_{rad} is the sum of the radiation intensity over all angles:

$$P_{\mathrm{rad}} = \int_{\Omega} U(\theta,\phi)\,\mathrm{d}\Omega \tag{2.14}$$

The pattern of the antenna is often described by its gain, $G(\hat{\boldsymbol{r}})$, the radiation intensity normalized with the input power:

$$G(\hat{\boldsymbol{r}}) = \eta_{\mathrm{r}}\frac{U(\hat{\mathbf{r}})}{U_{\mathrm{ave}}} = \eta_{\mathrm{r}}\frac{U(\hat{\mathbf{r}})}{P_{\mathrm{rad}}/4\pi} \tag{2.15}$$

where P_{rad} is the total radiated power and η_{r} is the radiation efficiency, which accounts for power dissipation of the antenna.

Finally, for a full description, the electric field created from the current carried on the radiating element will be derived. From Equations (2.1)-(2.4), the existence of a vector and scalar potential can be derived. The potentials lack direct physical meaning, but they are helpful as mathematical tools. For this task, the magnetic retarded vector potential $\boldsymbol{A}$ given a time-harmonic sources, is of use [13]:

$$\boldsymbol{A}(\boldsymbol{r}) = \mu_0 \int_\Gamma \frac{\boldsymbol{J}(\boldsymbol{r}')\mathrm{e}^{-\mathrm{j}k|\boldsymbol{r}-\boldsymbol{r}'|}}{4\pi|\boldsymbol{r}-\boldsymbol{r}'|}\,\mathrm{d}v' \tag{2.16}$$

where $\boldsymbol{J}(\boldsymbol{r}')$ is the current density at the evaluation point $\boldsymbol{r}'$ on the radiating structure Γ, and $\boldsymbol{r}$ is the observation point. $\boldsymbol{H}$ is related to the vector potential $\boldsymbol{A}$ as [13]:

$$\boldsymbol{H}(\boldsymbol{r}) = \frac{1}{\mu_0}\nabla \times \boldsymbol{A}(\boldsymbol{r}) \tag{2.17}$$

The far-field assumption is again helpful, and the distance between the observation point and evaluated point can be approximated as:

$$|\boldsymbol{r}-\boldsymbol{r}'| \approx r - \hat{\boldsymbol{r}}\cdot\boldsymbol{r}' \tag{2.18}$$

which allows the far-field vector potential to be expressed as:

$$\boldsymbol{A}(\boldsymbol{r}) \approx \frac{\mathrm{e}^{-\mathrm{j}kr}\mu_0}{4\pi r}\int_\Gamma \boldsymbol{J}(\boldsymbol{r}')\mathrm{e}^{\mathrm{j}k\boldsymbol{r}'\cdot\hat{\boldsymbol{r}}}\,\mathrm{d}v' \tag{2.19}$$

Next, to find the magnetic field from Equation (2.17), one needs to consider the curl of the vector potential. Recognizing that the phase variation dominates the spatial dependence, the following approximation is made:

$$\boldsymbol{H}(\boldsymbol{r}) = \frac{1}{\mu_0}\nabla \times \frac{\mathrm{e}^{-\mathrm{j}kr}\mu_0}{4\pi r}\int_\Gamma \boldsymbol{J}(\boldsymbol{r}')\mathrm{e}^{\mathrm{j}k\boldsymbol{r}'\cdot\hat{\boldsymbol{r}}}\,\mathrm{d}v' \approx \frac{-\mathrm{j}k\mathrm{e}^{-\mathrm{j}kr}}{4\pi r}\hat{\boldsymbol{r}} \times \int_\Gamma \boldsymbol{J}(\boldsymbol{r}')\mathrm{e}^{\mathrm{j}k\hat{\boldsymbol{r}}}\cdot\boldsymbol{r}'\,\mathrm{d}v' \tag{2.20}$$

Finally, the E-field can be expressed using Equation (2.7):

$$\boldsymbol{E}(\boldsymbol{r}) = \frac{-\eta_0\mathrm{j}k\mathrm{e}^{-\mathrm{j}kr}}{4\pi r}\hat{\boldsymbol{r}} \times \left(\int \boldsymbol{J}(\boldsymbol{r}')\mathrm{e}^{\mathrm{j}k\boldsymbol{r}'\cdot\hat{\boldsymbol{r}}}\,\mathrm{d}v' \times \hat{\boldsymbol{r}}\right) = \frac{\mathrm{e}^{-\mathrm{j}kr}}{r}\boldsymbol{F}(\boldsymbol{r}) \tag{2.21}$$

This shows that the electric field is the Fourier transform of the current on the radiating element, providing a helpful insight for antenna performance analysis.

An example of a hypothetical radiation pattern generated by a current directed along the x-axis is shown in Figure 2.1a, meant to illustrate a typical radiation pattern. The E-plane and the H-plane are the planes in which the fields vary [12], and with the direction depicted for the example, the E-plane is the xz-plane where $\phi = 0°$, and the H-plane is the yz-plane with $\phi = 90°$.

The Half-Power Beamwidth, HPBW, is defined as the angle at which the power in the main beam of the radiation is reduced to half its maximal amplitude [12], and is shown in Figure 2.1b. The HPBW, but also commonly referred to as θ_3 or ϕ_3 where the index 3 refers to a reduction of -3dB of the full beam amplitude.

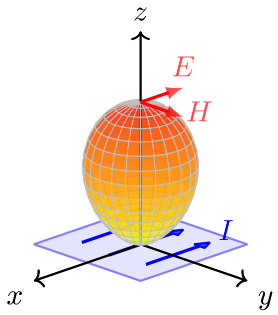

(a) Example of 3D radiation with E- and H-field directions.

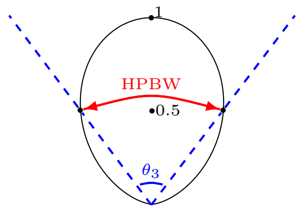

(b) 2D cut of 3D raditation pattern, with the HPBW depicted.

Figure 2.1: 3D and 2D radiation pattern.

The maximal gain of the antenna is directly proportional to the ability to direct energy in a certain direction. The value is thus highly dependent on the electrical size of the antenna and the value can be expressed as [11, p.313]:

$$G_{\max} = \eta_{\mathrm{r}} \frac{4\pi A}{\lambda^2} \tag{2.22}$$

where A is the antenna aperture area, and η_{r} the aperture efficiency factor. Following the same motivation the HPBW is inversely proportional to the maximal gain as [11, p.313]:

$$G_{\max} \propto \frac{1}{\theta_3 \phi_3} \tag{2.23}$$

The relationships emphasize that the antenna size, beam directivity, and maximal gain are interdependent, and often require careful consideration in antenna design.

2.2.2 Antennas as circuit elements

For efficient radiation, the same amount of power fed to the antenna must be accepted, which requires that the antenna is matched to the feed. This is measured by the reflection coefficient Γ [12]:

$$\Gamma = \frac{Z - Z_0}{Z + Z_0} \tag{2.24}$$

where Z and Z_0 is the antenna and feed impedance respectively. The feed impedance is commonly 50 or 75 Ω. The antenna impedance is [12]:

$$Z_0 = R_0 + \mathrm{j}X_0 \tag{2.25}$$

where R_0 is the antenna resistance and X_0 is the antenna reactance. Since the feed impedance is real valued, ideally the antenna should have zero reactance. If the antenna does not meet the required impedance, a matching network should be included.

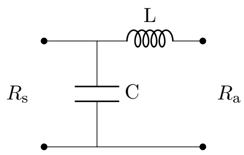

Figure 2.2: LC-matching network from a source with resistance R_{s} and a load, in this case the antenna, R_{a}. The figure is inspired from [14].

To match the reactance, this can often be achieved by introducing a capacitor or an inductor to cancel out the reactive component of the impedance. However, to match the resistance, components must be added without introducing significant losses. This can, for example, be done with an LC-network or a quarter wavelength ($\lambda/4$) transmission line.

The LC-network can be constructed as shown in Figure 2.2, and if $R_{\mathrm{s}} > R_{\mathrm{a}}$ the following equations can be used to obtain the component values for proper matching [14]:

$$Q = \sqrt{R_{\mathrm{s}}/R_{\mathrm{a}} - 1} \tag{2.26}$$

$$\omega C = \frac{Q}{R_{\mathrm{s}}} \tag{2.27}$$

$$\omega L = QR_{\mathrm{a}} \tag{2.28}$$

A $\lambda/4$ transmission line can also be used. The name refers to the transmission line length of a quarter wavelength of the carrier signal. For a circuit with a load impedance Z_{a} connected through a transmission line with characteristic impedance $Z_{0,\mathrm{c}}$, the input impedance Z_{in} at the other end is given by [15]:

$$Z_{\mathrm{in}} = \frac{Z_{0,\mathrm{c}}^2}{Z_{\mathrm{a}}} \tag{2.29}$$

Both of the matching techniques have minimal losses, depending on the quality of the components.

2.2.3 Bandwidth

The bandwidth is a range around the radiating center frequency where the radiation reaches a certain required performance. Usually for antennas, this is defined where the power reflection coefficient is less than 10 % (-10 dB) [12].

2.2.4 Image current theory

When a current is placed above a large ground plane, the EM wave reflection can be modeled as a mirror image current relative to the ground plane. The direction of the image current depends on the current direction compared to the ground plane. A current with a direction perpendicular to the ground plane produces an

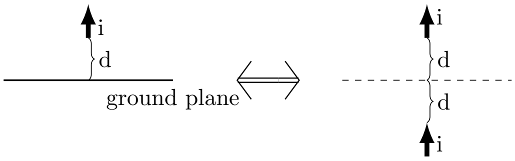

(a)

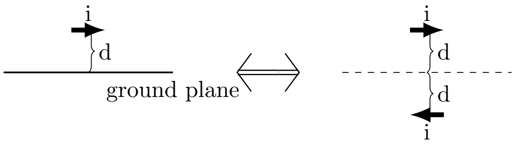

(b)

Figure 2.3: Image currents from a large ground plane for a perpendicular directed(a) and horizontal directed(b) current i in relation to the ground plane.

image current in the same direction as demonstrated in Figure 2.3a, whereas a tangential current will be mirrored in the opposite direction and is demonstrated in Figure 2.3b [12].

2.3 Phased Arrays

The performance of a radar system is highly related to the antenna. An electrically large antenna can direct radiation more efficiently, improving signal strength and allowing for better spatial detailing of the scene. To implement a large antenna, phased arrays can be used. The wave nature of the EM field ensures translation-phase-shift properties, and by considering placement and emission phase of each element, the radiation pattern is controlled.

The radiation vector $\boldsymbol{F}_\mathrm{a}(\hat{\boldsymbol{r}})$ and the gain $G_\mathrm{a}(\hat{\boldsymbol{r}})$ of the common antenna array pattern is scaled with the so-called Array Factor, AF [13]:

$$\mathrm{AF}(\hat{\boldsymbol{r}}) = \sum_{n=1}^{N} a_n \mathrm{e}^{\mathrm{j}(k\hat{\boldsymbol{r}}\cdot\boldsymbol{d}_n + \phi_n)} \tag{2.30}$$

$$\boldsymbol{F}_\mathrm{a}(\hat{\boldsymbol{r}}) = \boldsymbol{F}_\mathrm{e}(\hat{\boldsymbol{r}})\mathrm{AF}(\hat{\boldsymbol{r}}) \tag{2.31}$$

$$G_\mathrm{a}(\hat{\boldsymbol{r}}) = G_\mathrm{e}(\hat{\boldsymbol{r}})|\mathrm{AF}(\hat{\boldsymbol{r}})|^2 \tag{2.32}$$

where a_n is the excitation factor, $\boldsymbol{d_n}$ and ϕ_n is the position and phase of element n using an array of N elements, $\boldsymbol{F}_\mathrm{e}$ is the element radiation vector and G_e is the element gain.

The periodicity of the array factor (AF) can lead to constructive interference in unwanted directions, known as grating lobes. These grating lobes are typically avoided by ensuring that the element spacing is less than or equal to half the wavelength. However, according to Equation (2.22), the maximal gain, and

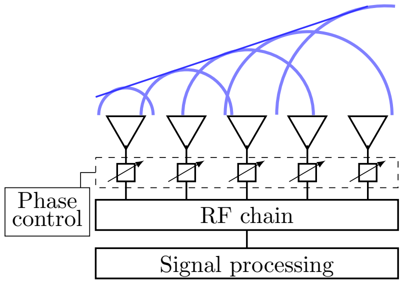

(a) PESA antenna

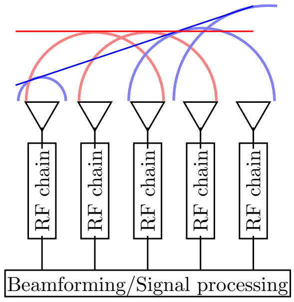

(b) AESA antenna

Figure 2.4: Platform based phased array, where relative phase difference between the elements can be adjusted. Depending on the phase of transmission from each element the position of the maximal amplitude of the transmission occur at different positions illustrated by the half-circle lines. The resulting superimposed wave from all elements is drawn with a horizontal line, and the propagation is perpendicular to this line. In (a) one RF chain is used and the beam is steered by phase shifters at each element. In (b) each element have its own RF chain and the phase and amplitude can be adjusted dynamically.

consequently the gain of the main lobe, increases as the effective aperture of the antenna array grows, which can result from increasing the element spacing.

When the spacing is increased in a sparse array configuration, grating lobes can be mitigated by breaking the periodicity of the element placement. This can be achieved by arranging the elements randomly. From a statistical point of view what is observed is that the main lobe gain increases linearly with the number of elements, N, while random noise introduced by the irregular spacing cause both the main lobe and side lobe gain to increase with N. The result is that the main beam gain increases N times more than the side lobe gain [16].

However, from a statistical point of view, the result can be misleading, as the random configuration can still cause beams to be directed in unwanted directions. Therefore, extensive research exists on determining the levels of the main lobe and the maximal side lobe, accounting for random element positioning [16][17][18].

The traditionally platform-based array can be controlled by the same transmitter/receiver by using phase shifters at each element to electronically steer the beam, the so-called passive electronically scanned array (PESA) [11], see Figure 2.4a. The active electronically scanned array (AESA) instead uses separate radio frequency (RF) chains and allows the phase and amplitude to be dynamically adjusted at each element, see Figure 2.4b [11]. The consequence of full signal control for each element is the possibility of faster beam adjustments, multiple beam capability, and higher system sensitivity. However, increasing the number of sensors requires more advanced processing, and communication and synchronization must be realized.

Instead of implementing antenna elements on a single platform, the antenna

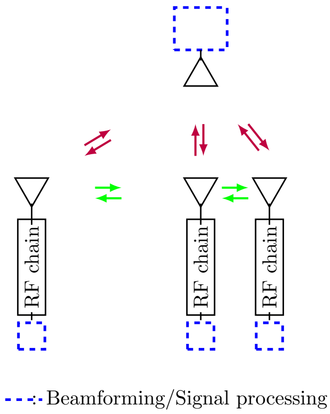

Figure 2.5: Distributed phased array, with 3 nodes. The synchronization is achieved wireless, and the location of the signal processing is therefore not strictly defined, illustrated by the dashed boxes. The synchronization can be centralized, with each node synchronizing on the same reference signal, either by an internal node of the array, or an external node and is illustrated with the purple arrows. Else it can be decentralized, where the nodes synchronize on a reference signal that is exchanged between nearby nodes, and is illustrated by the green arrows.

element along with a radio unit can be arbitrarily distributed in space. In the distributed phased array, the antenna element with its corresponding radio unit is often referred to as a node, and now synchronization must be achieved by wireless communication, as illustrated in Figure 2.5. For radar applications, the synchronization must be performed without target feedback, categorizing it as an open-loop synchronization [7]. This can be done by all nodes synchronizing on the same node, and is classified as a centralized open-loop or alternatively as a decentralized open-loop synchronization, where the synchronization is passed to a nearby node or nodes [19]. The two synchronization categories are illustrated with blue arrows in Figure 2.5. For the platform-based array, it is always assumed that the target is at a distance large enough for a common wavefront to form; this does not necessarily have to be the case for the distributed phased array. The distributed phased array can operate similarly to that of the AESA, but for either larger spacings between the nodes or directive element gain, the nodes can be used independently given that the signals add up in phase at the target destination. The signal incident on the target can then ideally be represented as [19]:

$$s_{\mathrm{i}}(t) = \sum_{n=1}^{N} W_n(t) \mathrm{e}^{\mathrm{j}2\pi f_c t} \tag{2.33}$$

where W_n is the transmitted waveform from element n, in an array consisting of N elements and f_c is the center carrier frequency. In reality, the uncertainty of position, time, carrier frequency and phase between the nodes makes precise synchro-

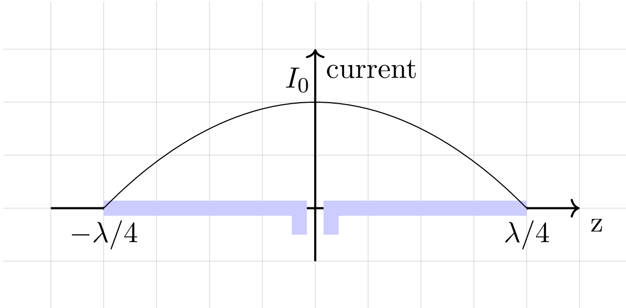

Figure 2.6: Current distribution of a half-wavelength dipole antenna at resonance.

nization challenging, and the constructive interference of the signal in Equation (2.33) is hard to achieve.

2.4 Half-wavelength Dipole Antenna

The half-wavelength dipole is a conducting rod, and as the name suggests, at resonance the length L is half a wavelength of the center frequency. The current distribution is shown in Figure 2.6 and can be expressed as:

$$\boldsymbol{J}(\hat{\boldsymbol{r}}) = \boldsymbol{J}(\hat{\boldsymbol{z}}) = I_0 \cos\left(\pi \frac{z}{L}\right) \delta(x)\delta(y)\hat{\boldsymbol{z}} = I_0 \cos\left(2\pi \frac{z}{\lambda}\right) \delta(x)\delta(y)\hat{\boldsymbol{z}}$$

where I_0 is the maximal current at the center of the dipole. The radiation vector in Equation (2.21), becomes:

$$\begin{aligned} \boldsymbol{F}(\hat{\boldsymbol{r}}) &= \frac{\eta_0 \mathrm{j}k}{4\pi} \hat{\boldsymbol{r}} \times \left(\iiint \mathrm{I}_0 \cos\left(2\pi \frac{z'}{\lambda}\right) \delta(x')\delta(y')\hat{\boldsymbol{z}} \mathrm{e}^{\mathrm{j}kz'\cos\theta} \, \mathrm{d}x' \, \mathrm{d}y' \, \mathrm{d}z' \times \hat{\boldsymbol{r}} \right) \\ &= \frac{\eta_0 \mathrm{j}k}{4\pi} \hat{\boldsymbol{r}} \times \left(\mathrm{I}_0 \hat{\boldsymbol{z}} \int_{-\lambda/4}^{\lambda/4} \cos\left(2\pi \frac{z'}{\lambda}\right) \mathrm{e}^{\mathrm{j}kz'\cos\theta} \, \mathrm{d}z' \times \hat{\boldsymbol{r}} \right) = \frac{i\eta_0 \mathrm{I}_0}{2\pi} \frac{\cos\left(\frac{\pi}{2}\cos\theta\right)}{\sin\theta} \hat{\boldsymbol{\theta}} \end{aligned}$$

The electric field will according to Equation (2.21) be proportional to the radiation vector, and the simplified radiation pattern is analyzed using Equation (2.13) as follows:

$$U(\hat{\mathbf{r}}) \propto r^2 \left|\boldsymbol{E}(\hat{\boldsymbol{r}})\right|^2 \propto r^2 \left| \frac{1}{r} \frac{\cos\left(\frac{\pi}{2}\cos\theta\right)}{\sin\theta} \right|^2 = \frac{\cos^2\left(\frac{\pi}{2}\cos\theta\right)}{\sin^2\theta} \tag{2.34}$$

Assuming a lossless antenna, with $\eta_r = 1$, the gain can be calculated using Equation (2.15), and the plotted result can be seen in Figure 2.7. The resulting pattern from a dipole is commonly described as a donut shape, but is more importantly omnidirectional in the azimuth direction. The maximum gain is at the center of the antenna perpendicular to its length, with a value of approximately 1.6 or 2.15 dB. The radiation resistance for this antenna is 73 Ω at resonance.

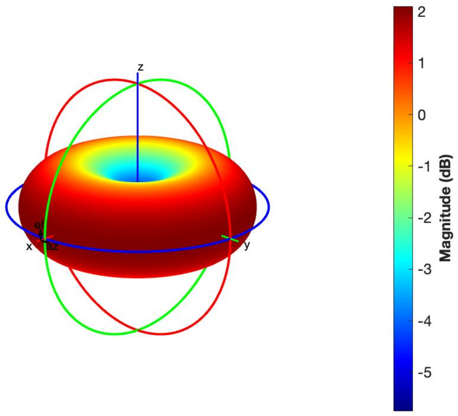

Figure 2.7: Gain of a lossless half-wavelength dipole antenna.

2.4.1 Feed

The half-wave dipole is usually fed in the center. In that configuration, each of the antenna rods share the same impedance, resulting in a balanced load seen by the feed. Supplying a balanced load with a balanced feed ensures that the same current flows through each antenna rod, as the current only has one way to flow, see Figure 2.8a where the equivalent circuit of a balanced feed is presented. In practice, an unbalanced coaxial cable is commonly used between the antenna and the source. The coaxial cable forces an equal, but opposite directed current on the inner conductor and on the inner side of the outer conductor. When the coaxial cable is connected with its outer conductor shield to the antenna, some current can leak on the outer side of the outer conductor, see Figure 2.8b. When the coaxial length approaches orders of the signal wavelength, the impedance of this path tends to decrease, resulting in the so-called common mode current of the coaxial cable being large [20]. The net current of the coaxial cable will radiate, and the typical current distribution on the dipole antenna is disturbed. Methods for increasing the impedance of the outer surface conductor current is done by a balun. The most common are the voltage-, current- and sleeve balun [20][12, p. 538].

2.4.2 Half-wave dipole antenna placed over a ground plane

A dipole directed perpendicularly to the ground plane in the xy-plane, at a distance $d\hat{\boldsymbol{z}}$, can be analyzed using image current theory, as the image current in Figure 2.3a suggests. The array factor from Equation (2.30) becomes:

$$\mathrm{AF}(\theta) = \mathrm{e}^{\mathrm{j}kd\cos(\theta)} + \mathrm{e}^{-\mathrm{j}kd\cos\theta} = 2\cos(kd\cos(\theta)) \tag{2.35}$$

The dipole gain, adjusted according to Equation (2.32), for $d = \lambda[0.1, 0.25, 1]$ is plotted in Figure 2.9. For a dipole that is parallel to the ground plane, the

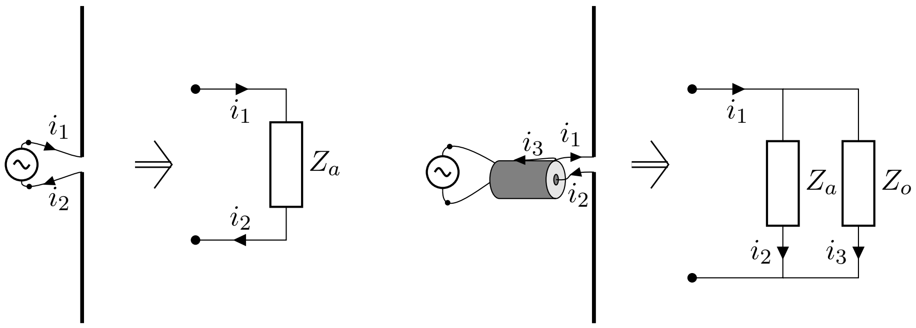

(a) Balanced feed **(b)** Coaxial (unbalanced) feed

Figure 2.8: Balanced- and coaxial feed to a dipole antenna with corresponding circuit representation.

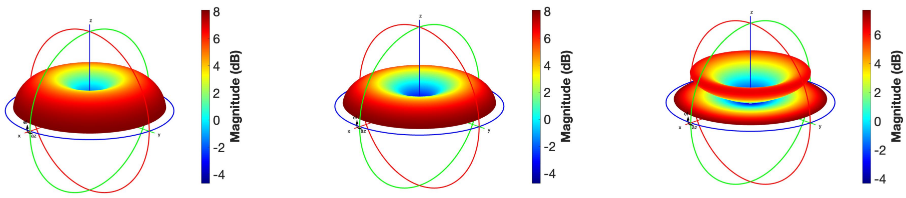

(a) $d = 0.1\lambda$ **(b)** $d = 0.25\lambda$ **(c)** $d = \lambda$

Figure 2.9: Vertical dipole placed above a ground plane in the xy-plane.

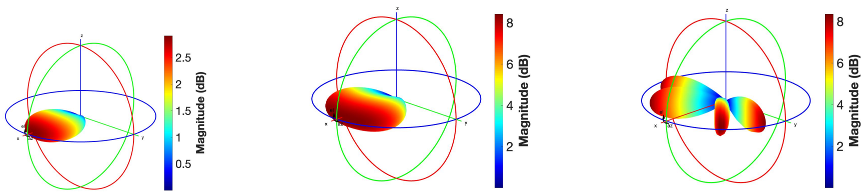

(a) $d = 0.1\lambda$ **(b)** $d = 0.25\lambda$ **(c)** $d = \lambda$

Figure 2.10: Horizontal dipole placed above a ground plane in the zy-plane.

plane is instead placed in the yz-plane to keep the radiation pattern of the dipole consistent. The dipole is placed in the z-direction at $d\hat{\boldsymbol{x}}$, and is instead modeled as in Figure 2.3b, and the array factor becomes:

$$\mathrm{AF}(\theta) = \mathrm{e}^{\mathrm{j}kd\sin(\theta)\cos(\phi)} - \mathrm{e}^{-\mathrm{j}kd\sin(\theta)\cos(\phi)} = 2\mathrm{j}\sin(kd\sin(\theta)\cos(\phi)) \tag{2.36}$$

The gain for the same distances d as for the vertical placed dipole, is plotted in 2.10.

2.5 Monopole Antenna

The quarter-wavelength monopole is a conducting rod placed perpendicularly to a ground plane. Assuming a large ground plane, in the far-field the monopole along with the mirror image current mimics a dipole antenna. The length of the quarter-wavelength monopole is therefore $L = L_{\text{dipole}}/2 = \lambda/4$.

The antenna's radiation is concentrated above the ground plane resulting in:

$$G_{\text{monopole}} = 2G_{\text{dipole}} \approx 3.2 \text{ or } 5.1 \text{ dB}$$
$$R_{\text{monopole}} = \frac{R_{\text{dipole}}}{2} \approx 36.5\ \Omega$$

Furthermore, the radiation pattern is similar to the one in Figure 2.9b.

2.6 Characteristic Mode Antenna

For a given conducting geometry, the current can be decomposed in a weighted sum of the eigencurrents supported by the structure [21]:

$$\boldsymbol{J} = \sum_n a_n \boldsymbol{J}_n \tag{2.37}$$

where $\boldsymbol{J}_n$ is an eigencurrent called the characteristic mode (CM) current, and a_n is the weight related to that mode, and is called the modal weighting (MW) coefficient.

With the geometry discretized with M elements the eigenvalue problem of the current on a geometry can be calculated as [22]:

$$\mathbf{X}\boldsymbol{J}_n = \lambda_n \mathbf{R}\boldsymbol{J}_n \tag{2.38}$$

where $\mathbf{X}$ and $\mathbf{R}$ are $M \times M$ sized matrices of the reactance and resistance, and λ_n is the eigenvalue corresponding to the eigencurrent $\boldsymbol{J}_n$. The presence of a mode is often measured by the modal significance MS and is defined as [21]:

$$\mathrm{MS}_n = \left| \frac{1}{1 + \mathrm{j}\lambda_n} \right| \tag{2.39}$$

When the mode is resonant, MS = 1, still the presence of a mode is significant when MS is greater than 0.7 [23].

The weighting coefficient a_n can also be calculated as [21]:

$$a_n = \frac{V_n^i}{1 + \mathrm{j}\lambda_n} \tag{2.40}$$

where V_n^i is the impressed modal excitation coefficient.

2.6.1 Feed

The key is to utilize the CM currents that will add up in Equation (2.37) to establish the desired radiation pattern. The mode can be excited, either inductive or capacitive, ideally by modifying the occurring modes as little as possible.

An inductive coupling element (ICE) is commonly an externally attached half-loop or integrated into the geometry with slots [22][24]. For the maximal coupling between the ICE feed and the CM, the placement should be in the position of the maximum current of the CM [24].

A capacitive coupling element (CCE) can be externally attached to the geometry, and the coupling to the CM is best when placed where the electric field distribution is the strongest, which coincides where the current of the CM is the smallest [25].

Chapter 3

System trade-off

Establishing clear goals for antenna performance is essential. This involves identifying potential radar system applications and defining metrics to guide the design and compare different antenna options. In parallel, the drone's limitations, such as possible carrying weight and space constraints must be considered, to ensure the chosen antenna meets both performance and practical implementation requirements. The following sections therefore evaluates what can be expected from commercial hardware to establish a framework for the radar application based on the radar range equation. The result from this will thereafter be used to evaluate potential application set-ups.

3.1 System Hardware

3.1.1 Carrier Platform

The radar system is analyzed by assuming integration in the DJI Matrice 100 commercial unmanned aerial vehicle (UAV). The drone was chosen for this project because it is available as a hardware resource through WARA-PS[1]. WARA-PS is a research initiative that provides support to various projects, making access to their resources possible. Matrice 100 is a rigid, carbon fiber quadcopter designed to handle a customizable load in different environmental conditions. Relevant specification is presented in Table 3.1[2], and the specification for the TB48D battery, commonly used by Matrice 100, is presented in Table 3.2[2].

3.1.2 Radio Unit

The radar functions will be implemented using a software-defined radio (SDR). The SDR utilizes software to control key characteristics that were traditionally managed by hardware, such as the frequency and bandwidth of the signal. This capability allows a single product to be highly versatile, supporting a wide range of use cases. While SDRs can typically generate low frequencies, they are limited at higher frequencies, with the current commercial SDRs' maximum frequency reaching up to 6 GHz. To summarize the expected performance for the SDR in

[1]WARA-PS: `https://portal.waraps.org/page/home`
[2]DJI Matrice 100 specs: `https://www.dji.com/si/support/product/matrice100`

Max angular velocity:	Pitch: 300°/s, Yaw: 150°/s
Max. speed of ascent:	5 m/s
Max speed of descent:	4 m/s
Max ready-to-fly altitude:	3000 m
Hovering time with TB48D battery and 500 g payload:	17 min
Hovering time with TB48D battery and 1 kg payload:	13 min
Diagonal wheelbase:	65 cm
Communication frequency:	5.725-5.825 GHz

Table 3.1: Relevant specifications of the DJI Matrice 100.

Capacity:	5700 mAh
Watt hours:	129.96 Wh
Voltage:	22.8 VDC

Table 3.2: Specification of TB48D battery.

the planned system, the most relevant specifications of four commercial SDRs are outlined in Table 3.3

The maximum power output of an SDR is frequency dependent, typically decreasing as the frequency increases [26]. Each of the SDRs listed has at least one transmitter port (Tx) and one receiver (Rx) port. The SDRs are connected via a USB interface, which handles both communication and power delivery. Each SDR unit incorporates a Field-Programmable Gate Array (FPGA) that can manage control tasks and perform some level of signal processing. However, depending on the complexity of the radar system, if the FPGA's resources are insufficient, an additional host system can be added. This will likely be a single-board computer (SBC), for instance, Raspberry Pi SBCs offer models with USB 3.0 connectivity. The details of communication between the SDR, the host on the drone, and the user are not within the scope of this project.

3.1.3 Parameter trade-off

The size of the drone imposes the first limitation on the frequency range. It is assumed that the antenna will be larger than a quarter wavelength, which results

[3] USRP: `www.ettus.com/wp-content/uploads/2019/01/b200-b210_spec_sheet.pdf`

[4] LimeSDR: `www.crowdsupply.com/lime-micro/limesdr`

[5] Matchstiq Z2: `www.everythingrf.com/products/software-defined-radios/epiq-solutions/957-983-matchstiq-z2`

[6] Blade RF: `www.nuand.com/bladerf-2-0-micro/#specification-wapper`

Model	Frequency	Power output	Inst. BW	Weight	Dimensions
USRP b210/b200[2]	70 MHz-6 GHz	$>$ 10 dBm	56 MHz	350 g	9.7x15.5x1.5 cm
LimeSDR[3]	100 kHz–3.8 GHz	10 dBm	61.44 MHz	49 g	10x6 cm
Matchstiq Z2[4]	45 MHz-6 GHz	10-13 dBm	50 MHz	200 g	8.74x6.20x1.42
Blade RF 2.0 micro[5]	47 MHz-3.8 GHz	-	56 MHz	90 g	6.3x10.2x1.8

Table 3.3: Specifications on four different SDRs.

in a frequency range of interest between 100 MHz and 6 GHz, with the SDR limiting the upper frequency. Additionally, the communication frequency used by the drone should be avoided.

All Raspberry Pi models have a peripheral current draw of less than 1.6 A[6]. Comparing this with the capacity of the TB48D battery:

$$\text{Batterytime} = \frac{5700\ \text{mAh}}{1600\ \text{mA}} = 3.56\ \text{h}$$

Given this worst-case result, the power consumption of the radar system will be much lower than that required to sustain the drone, so the drone's hovering time should not be significantly affected.

Based on the SDR weights listed in Table 3.3, we assume the SDR weighs approximately 200 g, while the Raspberry Pi SBC weighs 50 g[6]. This leaves a maximum of 750 g for the antenna and supporting components, such as feed cables, mounting hardware, and potential ground planes. However, since the hovering time decreases with increased weight, it is important to keep the total weight as low as possible.

The power output is assumed to decrease linearly from 13 dBm to 10 dBm across the frequency range, accounting for the frequency dependence of the output power.

3.2 Radar System trade-off

The foundation of the comprehensive but general analysis of the system is the radar range equation in Equation (2.10). Specifically, the parameters F, L_s, and the lowest limit of SNR are approximated using common values. The average power P_avg is derived from the hardware analysis, while T_d, G_r, G_t, and σ are estimated for specific scenarios. For each case, R is plotted for various λ within the frequency range determined by the hardware analysis.

Assuming negligible atmospheric losses, signal processing losses as well as transmit and receive losses are estimated to be on the order of 10 dB [11, p.67-69]. The noise figure is assumed to be approximately 10 dB, based on the USRP SDR specifications, which indicate a noise figure of less than 8 dB. The minimum SNR is set to 10 dB [11, p.565], and the average power P_avg is assumed to be 95% of the maximum power output.

The performance of the system will be analyzed based on the operating frequency, as several parameters depend on frequency. Finally, the radar waveform will be motivated, and the intended application will be determined.

3.2.1 Frequency Dependence of Radar Range Equation

To begin, two different antenna gains are evaluated. For this evaluation, the radar cross section is approximated based on the target object's area. In Figure 3.1, the target is a human with a radar cross section, $\sigma = 1\ \text{m}^2$. The coherent processing interval is set to $T_\mathrm{d} = 20$ ms, assuming that human motion is slow compared

[6]Raspberry Pi Documentation: `https://github.com/raspberrypi/documentation`

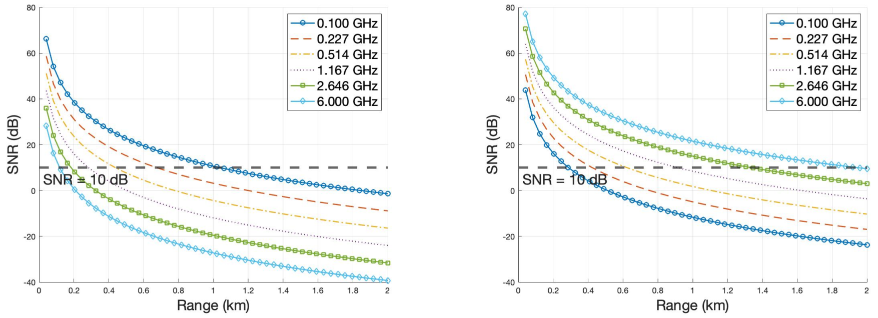

(a) Dipole antenna.

(b) Aperture antenna.

Figure 3.1: SNR plotted over range for frequencies between 100 MHz and 6 GHz. The minimum SNR is plotted, with interceptions indicating the maximum range for each frequency. In (a), a dipole antenna is used, and in (b), a 30x30 cm aperture antenna is used.

to the measurement speed. However, if the system speed needs to be increased, T_{d} needs to decrease. The radar range equation is plotted for a range of different frequencies, assuming two different antenna gains. In Figure 3.1a, a dipole antenna is used, providing a constant gain of 2.15 dB across all frequencies. In Figure 3.1b, a square aperture antenna with each side measuring 30 cm is used, resulting in a frequency dependent gain as described by Equation (2.22).

Next, attenuation losses of the signal generally increase with higher frequencies as the electrical distance increases and objects become electrically larger. To evaluate the potential attenuation effects across the given frequency range, an attenuation corresponding to 20 m propagation in woodland terrain according to the model presented in [27] is included. In this case, the human radar cross section is used along with the dipole antenna gain and the 20 ms coherent processing interval. The results, with and without woodland attenuation, are plotted in Figure 3.2.

Additional parameters that can vary with frequency include the coherent processing interval and the radar cross section. The coherent processing interval limits the system speed and is constrained by the target's decorrelation time, which measures how long the target can remain illuminated without changing noteworthy. For higher frequencies, this interval tends to decrease [11]. The radar cross section is frequency dependent because it reflects how electromagnetic waves interact with a target, considering factors such as amplitude, phase, material properties, and geometry. Its frequency dependence arises from effects like resonance, scattering mechanisms, and surface interactions, which vary with the wavelength relative to the target size and structure. Using a frequency with a wavelength comparable to the size of the target is a good starting point, as the scattering for wavelengths with orders larger than the object is typically small [11, p.142-143].

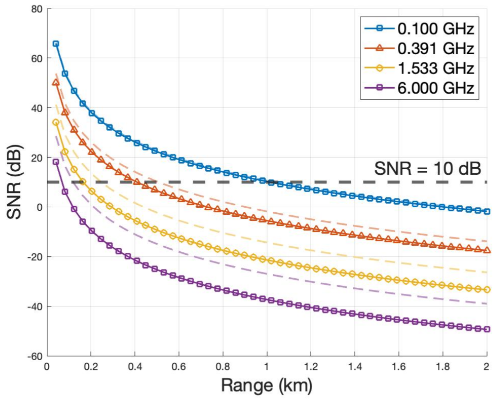

Figure 3.2: SNR plotted over range for frequencies between 100 MHz and 6 GHz, with 20 m woodland attenuation and the same result without attenuation (indicated by the faded dashed lines).

3.2.2 Phased Array Configuration

When a phased array with N elements is used in a radar system, the radar range equation is scaled by a factor of N^2, as the array forms a common wavefront. The dipole antenna, as shown in Figure 3.1a, is now depicted with $N = 10$ elements in Figure 3.3. For a common wavefront to form, the radiation pattern of each element must be broad enough for the radiated waves to combine coherently. The 30 cm radius aperture antenna shown in Figure 3.1b at 1 GHz will, according to Equation (2.22), have a maximum gain of approximately 12.6. Using Equation (2.23), assuming that the beam is equally wide in both directions, the beamwidth is approximately 17°, which may not be wide enough. Therefore, using an antenna with a more directed beam at each element would require steering the beam toward a common target. This could be achieved by either adjusting the direction of the drone or by incorporating steering electronics at each element.

The different configurations of the drone-based phased array are illustrated in Figure 3.4-3.6, where each drone represents one node.

Ideally, the same antennas used for radar system, would also serve for synchronization between the nodes. Depending on the radiation direction, either a centralized or decentralized synchronization approach must be considered. If the radiation between the nodes is sufficient, a decentralized approach would be efficient, while if for example the radiation is directed straight down and the radiation between two nodes is insufficient, synchronization could be performed on towards ground in a centralized configuration. To summarize depending on the final system implementation, synchronization strategies may need different configurations.

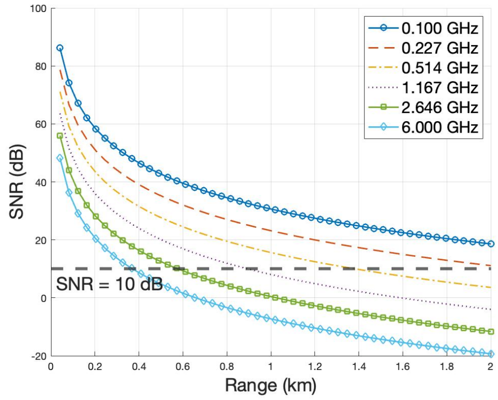

Figure 3.3: SNR plotted over range, using a phased array with dipole elements.

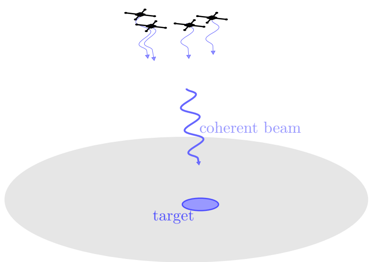

Figure 3.4: Radiation of each element forming common wavefront towards ground.

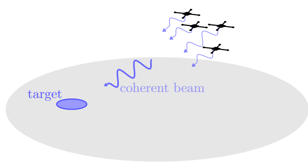

Figure 3.5: Radiation of each element forming common wavefront towards the side.

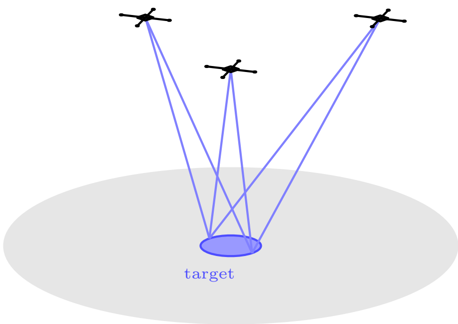

Figure 3.6: Radiation of each node add constructively first at the target

3.2.3 Radar Waveform

For a CW radar system implemented on the drone, the achievable isolation by physically separating the T_x and R_x antennas is limited. In the case of detecting a human target with a dipole antenna at a distance of 50 m, transmitting at 1 GHz, the condition for the received signal power P_r to equal the direct leakage power P_l can be analyzed as follows:

$$\begin{aligned}
&P_{\mathrm{r}} \approx P_{\mathrm{t}} \frac{G_{\mathrm{t}} G_{\mathrm{r}} \lambda^2 \sigma}{(4\pi)^3 R^4}, \\
&P_{\mathrm{l}} = P_{\mathrm{t}} |S_{12}|^2, \\
&\frac{P_{\mathrm{r}}}{P_{\mathrm{l}}} \geq 1 \Leftrightarrow |S_{12}| \leq \frac{G_{\mathrm{t}} G_{\mathrm{r}} \lambda^2 \sigma}{(4\pi)^3 R^4} = 7.4 \cdot 10^{-11} \approx -100 \text{ dB}.
\end{aligned}$$

Here, $|S_{12}|$ represents the signal leakage. Other methods for increasing isolation are outside the scope of this project and will not be considered.

For a pulsed radar waveform, additional parameters must be taken into account. To achieve high range resolution, the pulse width τ must be small, and is constrained by the minimum detectable range R_{min}:

$$\tau \leq \frac{2R_{\mathrm{min}}}{c}.$$

Furthermore, the target return from the maximum detectable distance R_{max} must be received within the PRI. Therefore, PRF must satisfy:

$$\mathrm{PRF} \leq \frac{c}{2R_{\mathrm{max}}},$$

where c is the speed of light.

3.2.4 Application

The primary advantage of a drone-based radar system is the dynamic control of the radar beam. For example, whether the signals from the nodes combine to form a common wavefront or add up constructively at the target position, the nodes can adjust their beams based on feedback. Drones can group into subarrays during search operations and reconfigure for tracking, depending on the required beam width. Similarly, each node can operate independently and communicate with others nodes, for example, when target classification requires illumination from an additional direction.

When a common wavefront is formed, constructive interference enhances the signal power, extending the detection range. This is illustrated in Figures 3.4 and 3.5. Directing the main beam sideways utilizes the increased range and allows for more detailed scene measurements. This setup is ideal for SAR applications, where images are reconstructed based on varying measurement ranges. It is also highly desirable in many search and track scenarios.

However, the full range does not always need to be exploited. Beams can also be directed downwards, where improved signal strength can be used to penetrate media with high signal losses. Such applications often require wideband radiation, necessitating synthetic increases in bandwidth of the SDR [28].

Finally, phased arrays allow targets to be illuminated from multiple directions simultaneously. In these cases, the signal strength from each node must be sufficient for the target location.

From the analysis, a frequency of 1 GHz is effective for achieving the desired detection range while maintaining acceptable attenuation properties. Its corresponding wavelength of 30 cm is manageable for drone implementation, as it allows for the integration of two antennas, one for transmission and one for reception. Consequently, the antenna design will focus on 1 GHz, targeting performance that aligns with the specifications in Figures 3.5 and 3.4.

Chapter 4

Simulation

4.1 Procedure

The project results are based on simulations performed using FEKO. Antenna designs integrated with the drone were developed as follows:

Drone Model All antennas must be analyzed in the presence of the drone. Therefore, a model was constructed in FEKO.

Antenna Design An investigation was conducted to identify potential antenna designs with the desired radiation characteristics, as well as size and weight properties. For each potential design, the following steps were carried out:

1. Design the antenna following established design rules.
2. Construct and analyze the antenna as a standalone model in FEKO.
3. Consider different placements of the antennas on the drone and simulate the antenna's performance in the presence of the drone.
4. Include the feed and arrangements to attach the antenna to the drone to evaluate their effects.

4.2 FEKO

FEKO is an electromagnetic simulation tool designed to solve Maxwell's equations of arbitrary geometric shapes. FEKO supports several frequency and time domain types of solver, and which one is used depends on the purpose of the analysis and complexity of the geometries.

For antenna design, when the geometries are of moderate electrical size and the materials are not too complex, the Method of Moments (MoM) solution method is an efficient and accurate solver type to use. It is a full-wave solution method, meaning it solves the Maxwell's equations by only discretizing the geometry body (not the free space). MoM solves the electromagnetic problem by calculating the currents of the geometry, which are then used to solve for the fields.

The workflow using FEKO starts in CADFEKO, where the model is constructed. There is extensive flexibility to build 3D shapes, using a variety of materials, including those provided by FEKO or custom materials defined by the user. Once the model is complete, the next step is to manage the solution settings and define the frequency range. For Standard and S-parameter configuration, ports and sources must be specified. FEKO provides a wide range of options for defining sources and ports. In addition, simple circuit elements can be added directly and external circuit networks can be imported and connected to the ports. In Characteristic Modes Configuration sources are not required. After defining sources (if applicable), requests for results are added. Common requests include Far- and Near-Field patterns and surface currents. The final step in CADFEKO is to run the simulation. Once the simulation is complete, the results are processed in POSTFEKO, where they can be visualized in 3D plots, Cartesian plots, polar plots, or Smith charts, depending on the type of result. Post-processing is also performed in POSTFEKO, with several built-in macros available. For example, in CM analysis, users can calculate the modal significance and excitation coefficients.

Chapter 5

Antenna Design

From the system trade-off analysis in Chapter 3, essentially two radar distributed phased array cases are identified, one having constructive interference at the target position and one where a common wavefront is formed. As mentioned, the first case mentioned required steering, either by tilting the drone or by electronics, and therefore, to start, the antenna will be designed to suit the common wavefront system to avoid that extra challenge.

The dipole and monopole antenna, essentially consisting only of a conducting rod, are relatively lightweight and the radiation pattern of each is omnidirectional in one direction. Therefore, these antennas are the first to be analyzed on the drone. The antennas are not known for having wide bandwidths, but considering the operational bandwidth of around 1 GHz compared to the bandwidth of the SDR of 50 MHz this will not necessarily be an issue. Although since the SDR's bandwidth can be synthetically increased methods for increasing the antenna bandwidth will also be considered.

Next, due to the weight and size constraints introduced by the drone, an analysis of the possibility and challenges of utilizing the drone itself as a characteristic mode antenna is executed.

In the next section, the model of the drone in FEKO is explained. The following sections present the analysis and results of the FEKO simulation of the antenna designs.

5.1 Modeling of the Drone

The model of the Matrice 100 constructed in FEKO included the body, the four arms, and the landing legs, closely following the true dimensions. The propellors were not included since modeling the rotation of the propellors would be very challenging. Whilst the motor is always placed in the center of the body, other attachable components are free to be placed either on top or under the drone body. For this model, only one battery is included at the top of the drone. The model in FEKO can be seen in Figure 5.1, from the top and from the side of the back. The figures also include a coordinate system, and if not else stated these are the coordinates used in following presented result.

The drone is built in carbon fiber material, but the exact material properties were not found and therefore the material was modeled as three different cases;

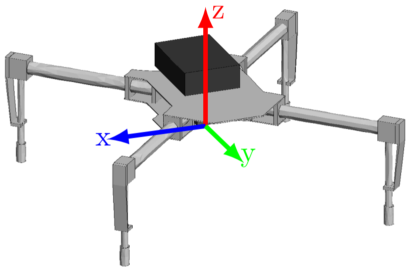

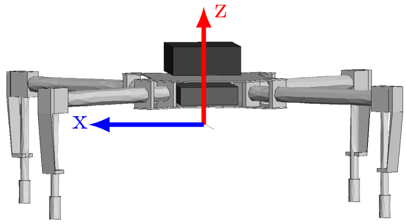

Figure 5.1: Model of DJI Matrice 100 in FEKO, from the top front and from the side of the back.

Material	A	B
ϵ_r	170	2.9
tanδ	0.38	0.04

Table 5.1: The extreme cases of carbon fiber electrical properties used to model the drone. Material A is based on carbon fiber-reinforced polymer, with the carbon fibers oriented in a direction relative to the incident electric field that yields the maximum relative permittivity ϵ_r and loss tangent tanδ. In comparison, Material B has the lowest possible ϵ_r and tanδ and is not reinforced by carbon at all.

a perfect electric conductor (PEC) and two cases of carbon fiber. The properties of the carbon fiber material were set in two extreme cases between neat resin and fiber reinforced polymer composites measured in [29]. The measurements covered 8-12 GHz, and not the frequency range of interest. Therefore, a rough approximation is performed, and the relative permittivity properties ϵ_r and the loss tangents tanδ used can be seen in Table 5.1, where the two extreme cases are referred to as Material A and B. Because of the rough approximation, rather than providing exact results, the two extreme cases provide an understanding of the potential influence of the carbon fiber compared to that of a PEC.

5.2 Dipole Antenna

The first half-wavelength dipole design presented includes the full iterative process; analysis of the antenna in the presence of the drone, feeding structure, and mounting arrangement. In the following sections, the results were obtained following a similar procedure, and to avoid repetition, only the final results are provided.

5.2.1 Dipole antenna horizontally placed under the drone

The first attempt was to place the antenna under the drone body, due to the ease of integration, and relatively protected location between the drone legs.

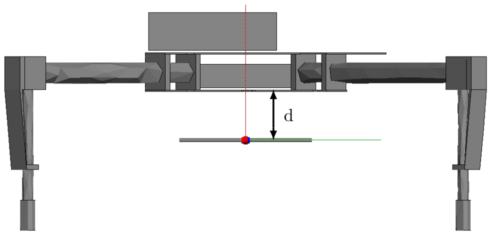

Figure 5.2: Single dipole antenna placed under the drone at a distance d from the drone body.

Dipole antenna in the presence of the drone

Initially, a half-wavelength dipole antenna was designed in free space in FEKO, with the aim of a resonance frequency around 1 GHz. The antenna was excited by placing a wire port and exciting it with a voltage source with resistance of 50 Ω. The resulting dipole had a resonance frequency at 0.98 GHz when L was set to 14 cm and the radius r was set to 1 mm, with typical dipole properties; 73 Ω resistance at resonance and an omnidirectional radiation pattern. The simplest case was to place the antenna centered under the drone modeled as a PEC, with the purpose of seeing how its properties changed and if the drone would resemble a ground plane. The dipole was placed at a distance $d = \lambda\,[0.18, 0.25, 0.33]$ from the drone body, and the drone and the dipole with the distance d depicted are shown in Figure 5.2. The resulting reflection coefficient and the real part of the impedance are plotted in Figures 5.3 and 5.4. In Figure 5.4, the imaginary part of the impedance is left out for visibility, and instead the center frequency of 0.946 GHz is indicated, where the corresponding imaginary part of the impedance for all three cases is close to zero. The resulting resonance frequency is slightly shifted to lower frequency for all cases, and the radiation resistance decreases as the distance d decreases. In Figure 5.5, the gain of the three cases is shown in the same coordinate system as the figures including the drone model at the resonance frequency of 0.946 GHz. The radiation pattern is more directive for shorter d, and when d becomes large enough several main beams start to appear, as the theory of a horizontally placed dipole above a ground plane also showed.

In summary, placing the dipole centralized under the drone does affect the radiation similarly to the theory of placing a dipole above a ground plane. Furthermore, since at some distances several main beams are introduced, these distances should be avoided.

Drone material effect

To evaluate the effect of the carbon fiber material of the drone body, the dipole antenna placed at a distance $d = 0.25\lambda$ was simulated for the two extreme case of material A and B from Table 5.1. The simulations showed that the reflection coefficient was barely affected and the result is plotted in Figure 5.6. The resulting gain in the H-plane and the E-plane is plotted in Figure 5.7. Material A shows

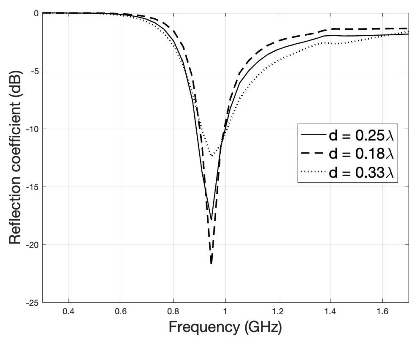

Figure 5.3: Reflection coefficient of dipole placed a distance d under the drone.

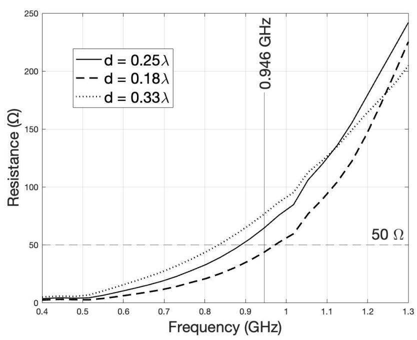

Figure 5.4: Real part of the dipole antennas impedance placed under the drone.

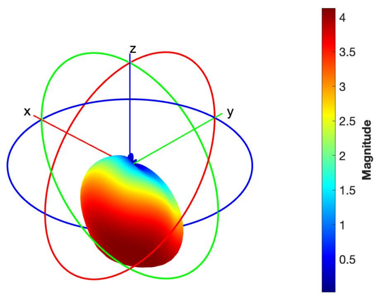

(a) $d = 0.25\lambda$

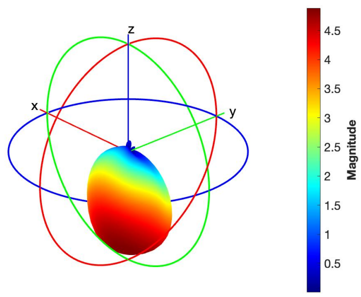

(b) $d = 0.18\lambda$

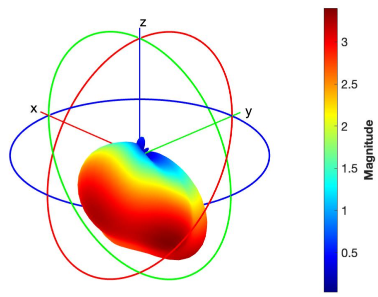

(c) $d = 0.33\lambda$

Figure 5.5: Radiation from a single dipole placed at different distances d under the drone at $f = 0.946$ GHz.

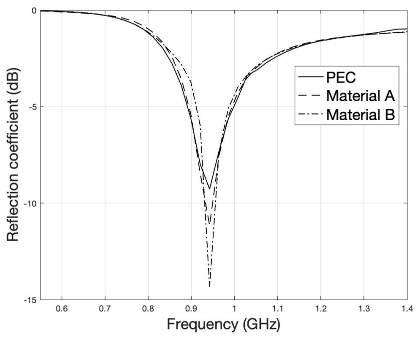

Figure 5.6: Reflection coefficient of dipole placed under the drone, modeled as a PEC and two extreme cases of carbon fiber.

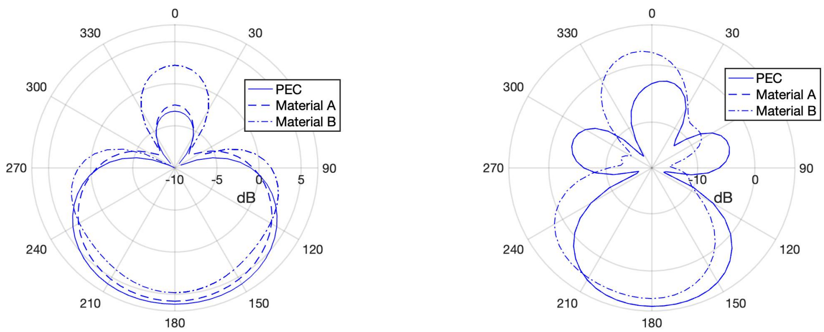

(a) H-plane

(b) E-plane

Figure 5.7: Gain of a single dipole under the drone modeled with different materials at 0.94 GHz.

a very similar radiation pattern, but with a slightly decreased maximal gain, and material B is similar, but less directed beam and with some radiation leakage to the other side of the drone body. In the E-plane plot the gain of the PEC case and material A case coincides.

In summary, the results are at the extreme values of carbon fiber but the results are just slightly shifted. Therefore, assuming that the drone can be modeled as a PEC when the dipole antennas are put under the drone is a reasonable assumption.

$\mathrm{R_x}$ and $\mathrm{T_x}$ dipole antennas placed parallel to each other along their vertical orientation.

The SDR has at least one $\mathrm{R_x}$ and one $\mathrm{T_x}$ port, therefore requiring two antennas. The placement of the dipoles parallel to each other, separated by a distance $s = [10, 15, 33]$ cm is illustrated in Figure 5.8, with both antennas having the same

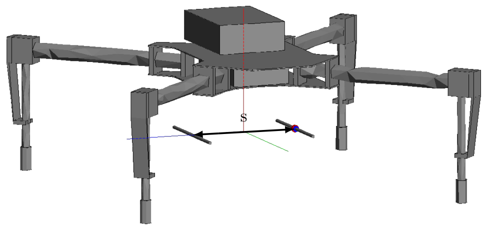

Figure 5.8: R_x and T_x dipole antennas placed a distance 0.25λ under the drone, separated by a distance s.

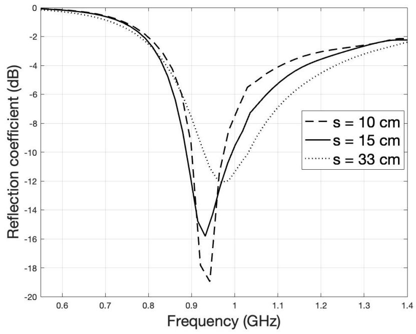

Figure 5.9: Reflection coefficient of parallel placed R_x or T_x antenna.

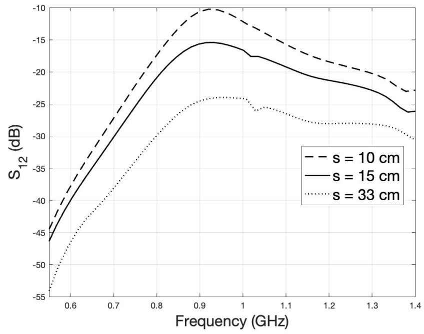

Figure 5.10: Signal leakage S_{12} between parallel placed R_x and T_x antennas.

dimensions as in the previous section. The separation distance s simulated corresponds to a half wavelength (0.15 cm), with a few cm added and subtracted. The idea is that the amplitude of the wave is to be at its minimum at the neighboring antenna for minimal reflection and absorption. The simulations were performed with added ports on each of the dipoles, with only one of them being excited. The simulated reflection coefficient and signal leakage are plotted in Figure 5.9 and 5.10, and has a center frequency around 0.94 GHz. The result shows that increasing the distance between the elements is the main contributor to reducing signal leakage. However, the distance that the antennas can be separated is restricted by the size of the drone, and as s increases, the results approach the characteristic of the dipole placed in free space and the reflection coefficient at resonance is increased.

Additionally, the gain in the E- and H-plane for the different s are plotted in Figure 5.11 at approximately $f = 0.94$ GHz. Since the maximal gain is slightly shifted towards the opposite direction as the neighboring antenna, some reflection does occur.

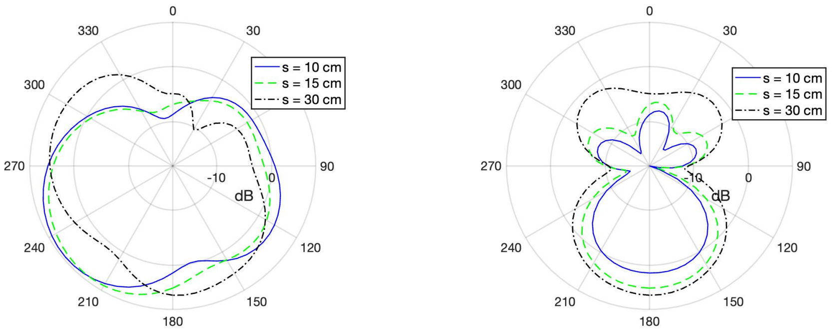

(a) H-plane **(b)** E-plane

Figure 5.11: E- and H-plane gain with the $\mathrm{R_x}$ and $\mathrm{T_x}$ antennas separated by a distance s, all at approximately $f = 0.94$ GHz.

Coaxial cable feed

Most antennas need to be compatible with coaxial cables which are therefore incorporated in the simulations. The modeled coaxial cable has an outer conductor radius of 2.1 mm, an inner conductor radius of 0.65 mm and a substrate with relative permittivity $\epsilon_\mathrm{r} = 2$. The dimensions were approximated aiming for a characteristic impedance Z_0 of 50 Ω using the following formula [15]:

$$Z_0 = \sqrt{\frac{\mu}{\epsilon(2\pi)^2}}\ln(\frac{b}{a}) \approx 60\frac{\ln(\frac{b}{a})}{\sqrt{\epsilon_\mathrm{r}}} \tag{5.1}$$

with a and b being the inner and outer conductor radius respectively.

For this example, the distance $d = 5.7$ cm, $s = 15$ cm, $L = 14$ cm and $r = 0.8$ mm. The coaxial cable was connected so that one end from the center of the dipole was connected to the inner conductor of the coaxial cable and the other end to the outer shield. The coaxial cable extended to the point where the drone body starts. On each of the coaxial cables, a waveguide port was added, and one of them was excited. The result of the simulations showed a great change in both the reflection coefficient and radiation pattern compared to the wire port fed dipole, and currents on the coaxial cable outer shield were directed in two directions. This indicates that the common mode on the coaxial cable is large and therefore problematic. The reflection coefficient is shown in Figure 5.12 and an example of the gain at 1.05 GHz is shown in Figure 5.13.

The idea of blocking the common mode is to add a balun, and there exist several different commercial ones for the given frequency range. To model the balun a voltage balun was added. The voltage balun is a transformer with one inductor added between the inner and outer conductor of the coaxial cable and the other inductor at the center of the dipole, in a 1:1 ratio. The result of adding a balun is also included in Figure 5.12. The reflection coefficient and the gain with a coaxial cable feed with a balun and a wire port feed are plotted in Figure 5.14 and Figure 5.15. The resonance frequency shifts slightly to a lower value when

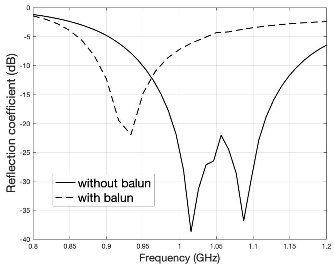

Figure 5.12: Reflection coefficient with and without a balun.

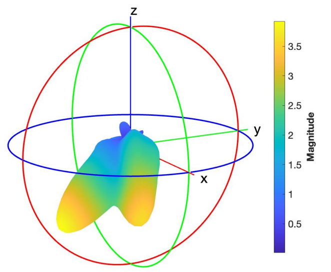

Figure 5.13: Example of the gain at f = 1.05 GHz for the dipole fed by a coaxial cable without a balun.

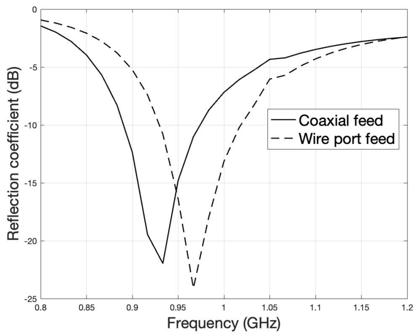

Figure 5.14: Reflection coefficient with a coaxial feed with an added balun and with a wire port.

switching to a coaxial cable feed. However, both feeds have similar bandwidths, with 84 MHz for the wire port and 89 MHz for the coaxial cable feed, and their gain is almost identical.

Mounting arrangement

The dipoles must be attached efficiently to the drone. Plastic has similar electric properties, and assuming a cylinder of plastic with $\epsilon_r \approx 2$ and $\tan\delta = 0.005$ around the coaxial cable, the dipole piercing through its center can be seen in Figure 5.16.

The resulting simulations of the reflection coefficient with and without mounting arrangement are presented in Figures 5.17 and 5.18. The result shows that attaching the dipole at the center using plastic results in a less well-matched antenna with the resonance slightly shifted to higher frequencies. However, the gain with and without the center mounting arrangement is almost identical.

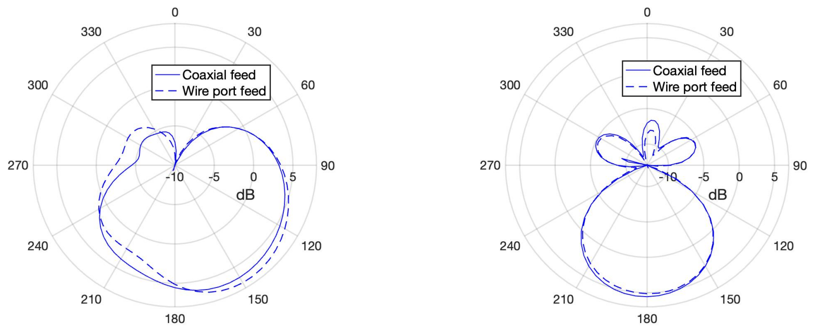

(a) H-plane **(b)** E-plane

Figure 5.15: E- and H-plane gain with coaxial cable feed and wire port feed at their corresponding resonance frequency, 0.93 GHz and 0.97 GHz respectively.

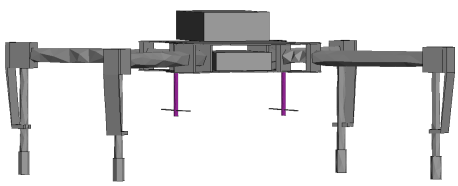

Figure 5.16: Drone with the cylindrical plastic hangers around the coaxial cable feed with the dipole attached at its center.

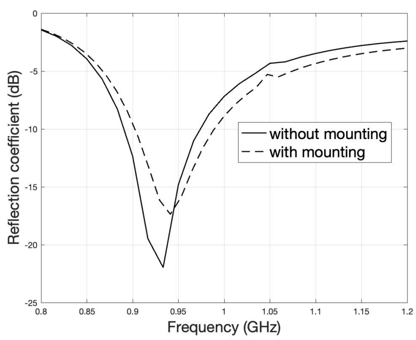

Figure 5.17: Reflection coefficient with and without the mounting arrangement included.

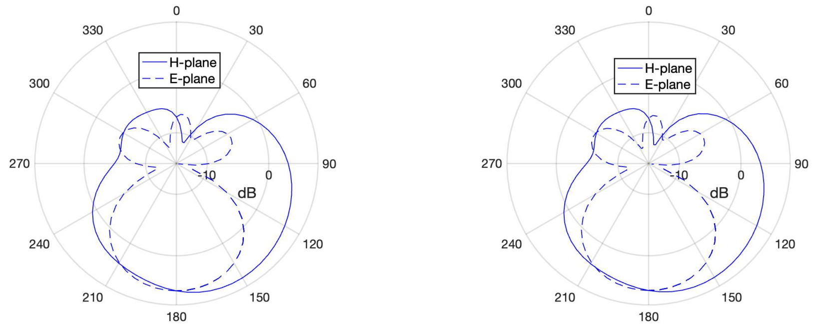

(a) **(b)**

Figure 5.18: 2D radiation remains very similar without (a) and with (b) mounting arrangement, with both at $f = 0.95$ GHz.

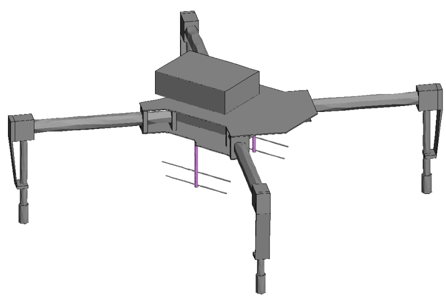

Figure 5.19: Dipole with parasitic element placed under the dipole to increase bandwidth. Similar mounting arrangement as previous section is extended to also carry the parasitic element.

Increasing bandwidth

One way to increase the bandwidth is to include parasitic elements. Furthermore, by carefully considering the placement of structures around the driven element, the induced currents on the parasitic elements can themselves radiate and are used to increase gain and/or bandwidth. Such a parasitic conducting rod, with the length slightly shorter than the fed dipole was added under the dipole, see Figure 5.19. A few iterations were performed to find the distance between the driven dipole and the parasitic element that yield sufficient results, and the final reflection coefficient, signal leakage and gain are plotted in Figures 5.20, 5.21 and 5.22. The figures also include the dipole without the parasitic element, with length L slightly adjusted to have a resonance frequency that includes 1 GHz within the bandwidth. From the figures the bandwidth is obtained as 170 MHz and 104 MHz with and without the parasitic element. The gain of the two is very similar and the same HPBW is assumed for the two cases, and are measured from the plotted gain as 132° in the H-plane and 76° in the E-plane. The maximal gain without

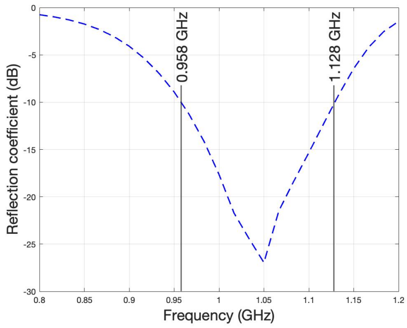

(a) With parasitic elements

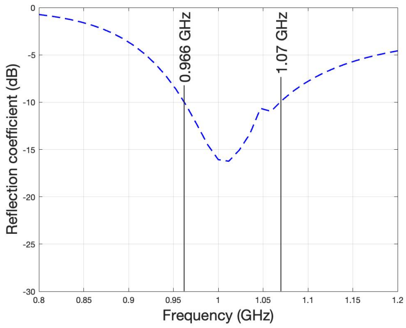

(b) Without parasitic elements

Figure 5.20: Reflection coefficient of dipole antennas placed parallel along their vertical orientation. The frequency where the reflection coefficient is -10 dB is indicated with vertical lines.

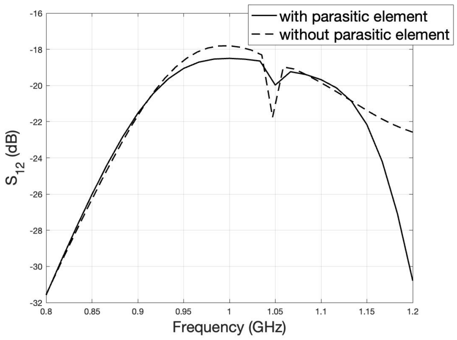

Figure 5.21: Signal leakage between $\mathrm{R_x}$ and $\mathrm{T_x}$ dipole antennas placed parallel along their vertical orientation with and without parasitic element.

the parasitic element is 6.1 dB and with the parasitic element 6.4 dB.

5.2.2 Dipole antenna horizontally placed under the drone, parallel to each other along their length

The dipoles and the parasitic elements were rotated so that they were parallel to each other along their lengths. The distance between them was increased as much as possible, still allowing the mounting arrangement to be connected to the drone body above. The aim was to reduce signal leakage. The reflection coefficient, signal leakage and gain are plotted in Figures 5.23, 5.24 and 5.25. The bandwidth was obtained from the plot in Figure 5.23 as 147 MHz. The HPBW was obtained from Figure 5.25 as 57° in the E-plane and 127° in the H-plane, with a maximal gain of 5.8 dB. Notice that, as the dipoles have different directions from the section

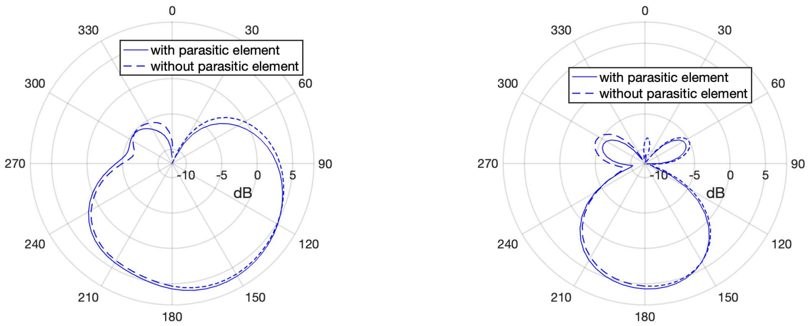

(a) H-plane **(b)** E-plane

Figure 5.22: Gain of dipole antennas placed parallel along their vertical orientation with and without parasitic element, at $f =$ 1 GHz.

above, the E- and H-planes are switched.

5.2.3 Horizontally parallel placement in front of the drone

To obtain a radiation to the side of the drone instead of under the drone the antenna was moved to the front of the drone and a ground plane was added. In the simulations the ground plane was modeled as a PEC rectangle, but in real life a chicken wire metal grid can be used as long as the grid holes are small enough in comparison to the operational wavelength. This will keep the weight as small as possible.

The first design had the placement of the dipole along with the parasitic elements suspended between the front legs of the drone. The mounting arrangement consists of the same material as modeled in previous sections, between the legs and the end of the drone, as well as in between the R_x and T_x antennas, see Figure 5.26. The resulting reflection coefficient, signal leakage and gain at $f =$ 1 GHz is plotted in Figure 5.27, 5.28 and 5.29. The bandwidth is obtained from the reflection coefficient as 171 MHz and the HPBW from the gain plot as 135° and 77° in the H- and E-plane respectively. The gain remained similar for the full bandwidth range with a maximal value of 4.2 dB.

In the second design, the dipoles were left under the drone, but shifted further down, with a ground plane added behind and the parasitic elements moved to the front. The placement of the ground plane can be motivated since attachable components (such as the battery) of the drone can also be placed under the drone, rather than at the top. The mounting arrangement is similar to that of the dipole placement under the drone, but an additional arrangement must be provided for the parasitic elements, see Figure 5.30. The resulting reflection coefficient, signal leakage, and gain are plotted in Figures 5.31, 5.32 and 5.33. The bandwidth is obtained from the reflection coefficient as 140 MHz and the HPBW from the 2D gain plot as 120° and 68° in the H- and E-plane respectively. Similarly to

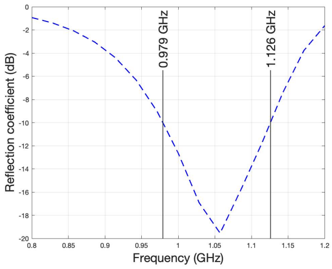

Figure 5.23: Reflection coefficient with $\mathrm{R_x}$ and $\mathrm{T_x}$ dipole antennas placed parallel along their length. The frequency where the reflection coefficient is -10 dB is indicated with vertical lines.

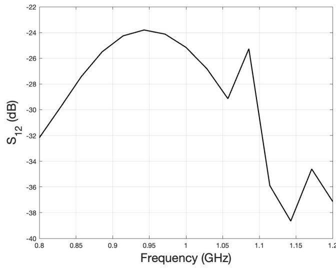

Figure 5.24: Signal leakage between $\mathrm{R_x}$ and $\mathrm{T_x}$ dipole antennas placed parallel along their length.

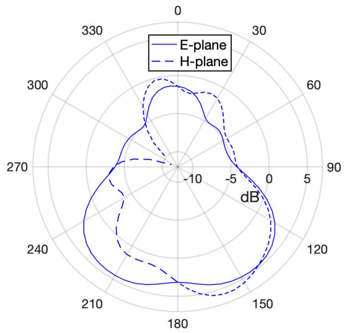

Figure 5.25: Gain of the $\mathrm{R_x}$ and $\mathrm{T_x}$ dipole antennas placed parallel along their length, at $f = 1$ GHz.

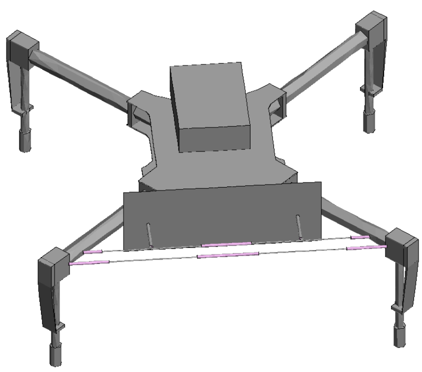

Figure 5.26: The dipoles and parasitic elements suspended using plastic attachments between the drone front legs.

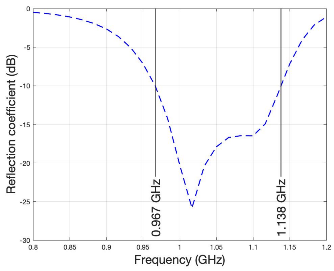

Figure 5.27: Reflection coefficient with $\mathrm{R_x}$ and $\mathrm{T_x}$ dipole antennas with parasitic elements suspended in front of the drone. The frequency where the reflection coefficient is -10 dB is indicated with vertical lines.

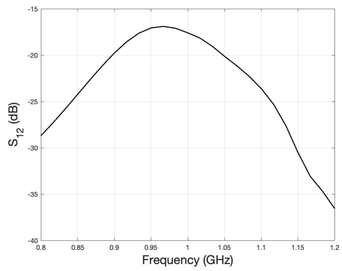

Figure 5.28: Signal leakage between $\mathrm{R_x}$ and $\mathrm{T_x}$ dipole antennas placed parallel along their length with parasitic elements, suspended in front of the drone.

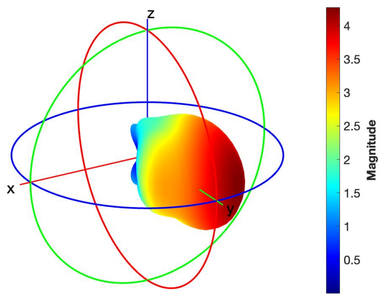

(a)

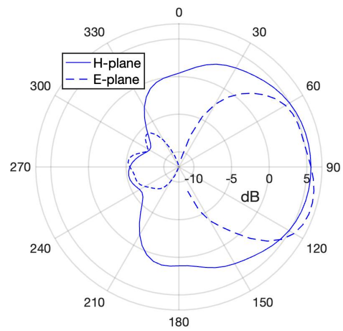

(b) E-plane

Figure 5.29: The 3D (a) and 2D (b) gain of a dipole with parasitic element at $f = 1$ GHz, suspended in front of the drone.

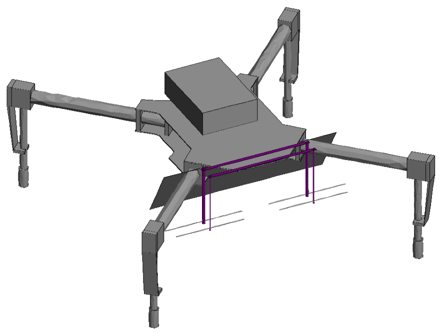

Figure 5.30: The dipoles and parasitic elements placed under at the front of the drone.

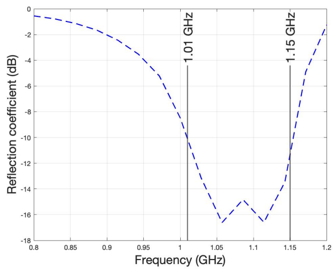

Figure 5.31: Reflection coefficient with R_x and T_x dipole antennas with parasitic elements, placed under at the front of the drone. The frequency where the reflection coefficient is -10 dB is indicated with vertical lines.

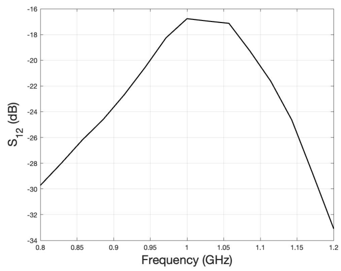

Figure 5.32: Signal leakage between R_x and T_x dipole antennas placed parallel along their lengths, with parasitic elements, placed under and at the front the front of the drone.

the first implementation, the gain remained similar for all frequencies within the bandwidth, with a maximal value of 4.3 dB.

5.3 Monopole Antenna

When a monopole antenna is constructed on a finite ground plane, the radiation pattern is significantly affected. Initially, a single monopole antenna was designed to resonate around 1 GHz, using a circular ground plane with a radius of 0.83λ. This size was chosen because it is close to the maximum that could fit on the drone. The resulting radiation pattern is shown in Figure 5.34a.

Subsequently, the antenna was placed on the drone, positioned close to the body of the drone. The corresponding radiation pattern, shown in Figure 5.34b, reveals that the radiation is strongly influenced by the presence of the drone legs.

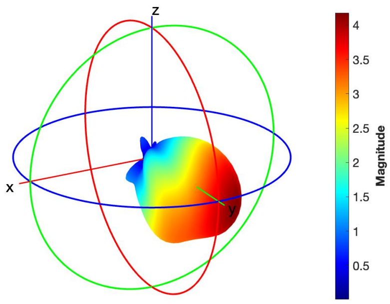

(a)

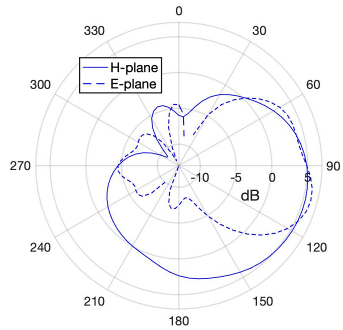

(b) E-plane

Figure 5.33: The 3D (a) and 2D (b) gain of a dipole with parasitic element at $f = 1$ GHz, placed under and at the front of the drone.

To mitigate this effect, the ground plane was moved further down, leading to an improved radiation pattern seen in Figure 5.34c. The single monopole with the ground plane under the drone is shown in Figure 5.35a.

Since the SDR requires two antennas, an additional monopole antenna was added, and is shown in Figure 5.35b. However, after several iterations to optimize the distance between the antennas, the result showed that the two antennas inevitably interfered significantly with each other. This interaction, as well as the lack of symmetry, resulted in multiple main beams, as shown in Figure 5.34d. Yet achieving these results required an awkward integration on the drone, involving a large ground plane placed far below the drone body. Due to these challenges, including the impractical integration and the effects on the radiation pattern, the monopole antenna was not further analyzed.

5.4 Characteristic Mode Antenna

Compared with the antennas in the above sections, a CM antenna functions when the presence of the CM is significant. Therefore, rather than adjusting this antenna to operate at around 1 GHz the following analysis investigates at what frequencies this antenna would be efficient and specifically provides an understanding of the lower limit of the frequency that the radar system on the drone would be able to operate at.

5.4.1 Characteristic modes of the drone

A model of the drone without additional components was used to carry out the analysis. The front of the drone was now instead directed in the x-direction. Since the geometry of the drone is quite complex, it supports a large number of modes. To find the lowest frequency carried by the drone, initially the CM configuration was simulated at a wide range of frequencies. The lowest modes were identified at

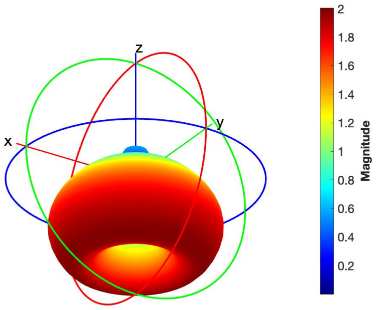

(a) Single monopole with ground plane that will fit on the drone.

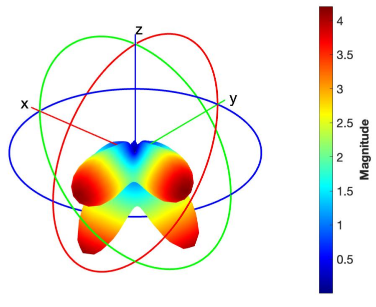

(b) Single monopole placed directly under the drone body.

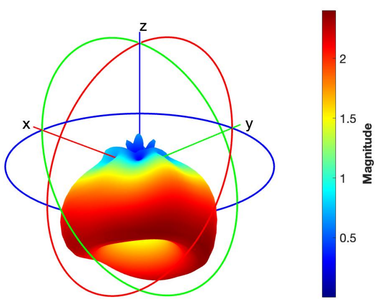

(c) Single monopole shifted down from the drone body.

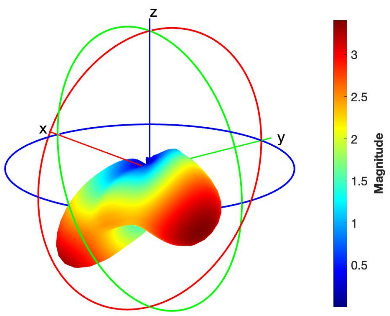

(d) $\mathrm{R_x}$ and $\mathrm{T_x}$ monopole antennas shifted down from the drone body.

Figure 5.34: 3D gain of monopole antenna either alone or integrated on the drone. The figures follows the iteration of attempting to implement the monopole antennas on the drone.

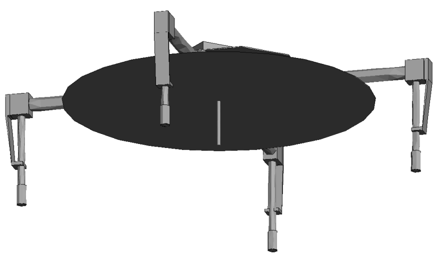

(a) Single monopole placed directly under the drone body.

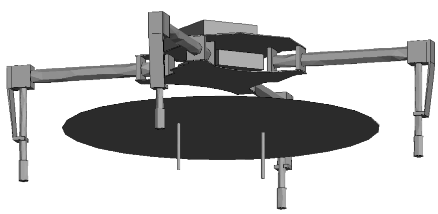

(b) $\mathrm{R_x}$ and $\mathrm{T_x}$ monopole antennas shifted down from the drone body.

Figure 5.35: Two of the attempted cases of implementing the monopole antenna on the drone.

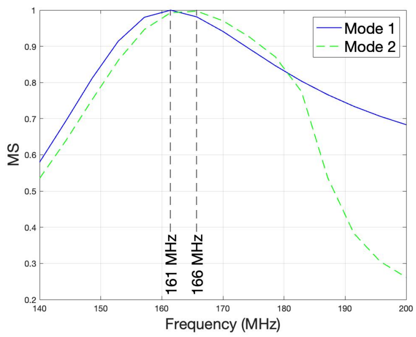

Figure 5.36: MS of mode 1 and mode 2.

around 160 MHz and the MS of the two lowest modes are plotted in Figure 5.36 over the relevant frequency range. The corresponding currents for the two modes are presented in Figure 5.37.

The CM current distribution of mode 1 and 2 are similar to two parallel dipoles on either side of the drone. Considering the radiation resulting from a dipole the potential of utilizing both modes to have a radiation covering the entire volume around the drone seems promising.

The maximum current of each mode is at the center, along the edges of the drone body. The maximal coupling of the ICE feed is at the current maximums. In addition, both modes also have weak currents at the center of the body, potentially allowing the radar equipment to be placed and connected to the ICE seamlessly.

The following sections examine the possibility of exciting the modes using an ICE. The first section analyses both mode 1 and mode 2, with the drone model as a PEC. The following section only covers exciting mode 1 with the drone modeled in carbon fiber.

5.4.2 Exciting modes assuming PEC drone

The ICE was fed by a wire port at the start of each ICE wire, as shown in Figure 5.38 for exciting mode 1 and 2. The MS was not influenced by adding the ICE and still reached a value of 1 at 161 and 166 MHz for the two modes respectively. Since both the ICE wire and the drone is modeled as PEC the resistance is very low, and therefore the loop wire is extended as long as possible along the sides of the drone.

The resistance of exciting mode 1 is shown over the relevant frequency range in Figure 5.39 and the reactance was around 280 Ω. Since the drone is symmetric in the xz-plane, the impedance and reflection coefficient of the two feeds were identical. The results shows that the ICE feeds are very poorly matched, however, the resistance increases at 160 MHz, and demonstrates that a mode is coupled. This is further confirmed in Figure 5.40, where the MW coefficient is increased at 160 MHz, still being low due to the poor matching.

To match the ICE, an LC-network and a double $\lambda/4$ transmission line were added along with a series capacitor between the port and the antenna. The values

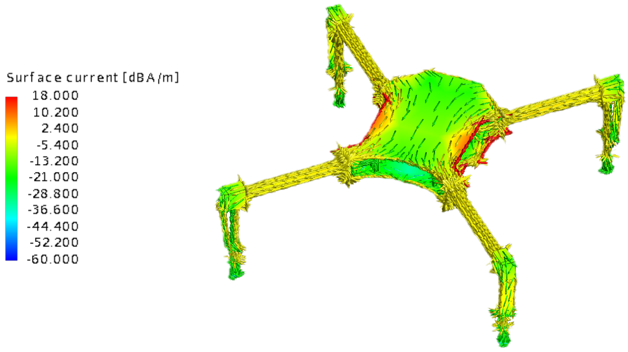

(a) Mode 1 at 161 MHz

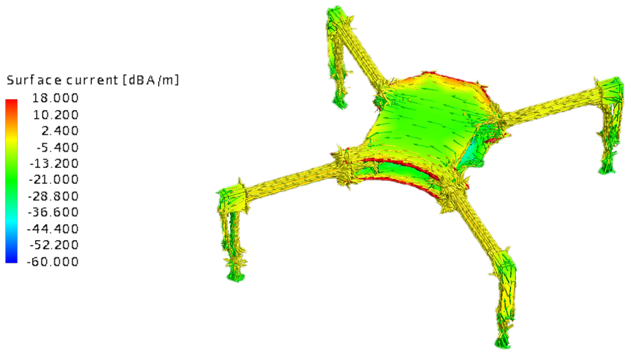

(b) Mode 2 at 166 MHz

Figure 5.37: CM currents on the drone modeled as PEC.

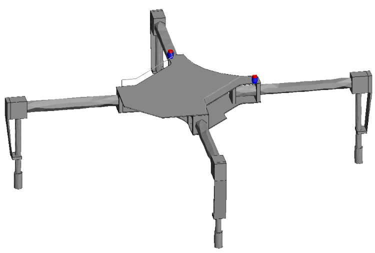

(a) Mode 1

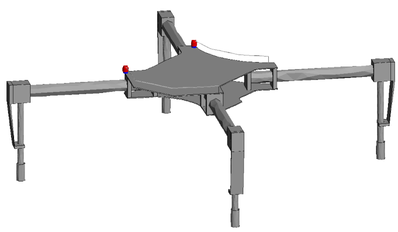

(b) Mode 2

Figure 5.38: ICE with feeds at the start of each wire, to excite mode 1 and mode 2.

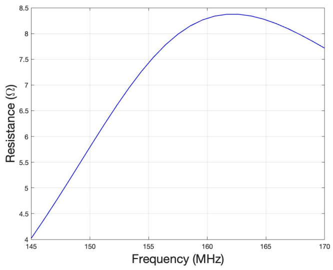

Figure 5.39: Resistance of mode 1 with the ICE feeds.

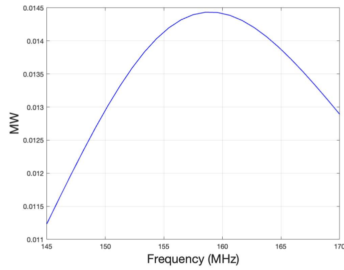

Figure 5.40: MW coefficient of mode 1 with the ICE feeds.

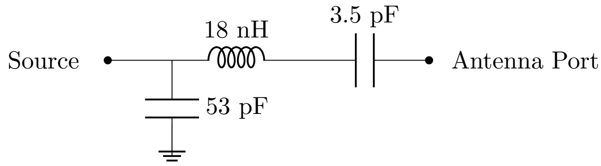

(a) LC-network matching with a capacitor in series.

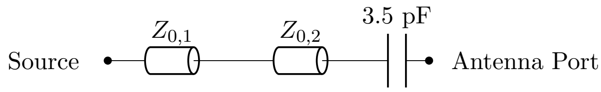

(b) Double $\lambda/4$ transmission line matching with $Z_{0,1} = 50\ \Omega$ and $Z_{0,2} = 125\ \Omega$, with a capacitor in series.

Figure 5.41: Matching networks for the ICE used to excite mode 1.

of the components in the LC-network were approximated using Equations (2.26) -(2.28). To find appropriate transmission line impedances Equation (2.29) was adjusted to account for the added transmission line:

$$Z_{\mathrm{s}} = \frac{Z_{0,\mathrm{c},2}}{Z_{0,\mathrm{c},1}} Z_{\mathrm{a}} \tag{5.2}$$

where $Z_{0,\mathrm{c},1}$ and $Z_{0,\mathrm{c},1}$ is the transmission line closes to the antenna port and closest to the source respectively. The networks with component values are summarized in Figure 5.41.

The resulting reflection coefficient and the MW coefficient are plotted in Figures 5.42 and 5.43. Since the maximum value of the MW coefficient using the double $\lambda/4$ transmission line matching coincides with the resonance frequency, the BW is obtained as 2.7 MHz and the gain is plotted in Figure 5.44 of this version.

The same procedure is carried out for mode 2, although now the drone is no longer symmetric on either side of the ICE placement. The resistance and MW coefficient are plotted in Figures 5.45 and 5.46.

Similar LC-matching network techniques as used for matching the ICE feeds of mode 1 were attempted, to adjust the resistance of each of the feeds, and the resulting reflection coefficient is shown in Figure 5.47. The reflection coefficient in

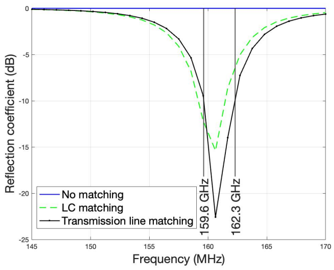

Figure 5.42: Reflection coefficient of mode 1 with and without matching. The -10 dB reflection coefficient is depicted using transmission line matching.

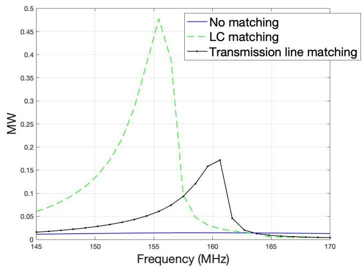

Figure 5.43: MW coefficient of mode 1 with and without matching.

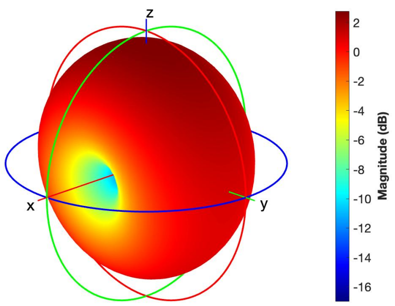

Figure 5.44: Gain of mode 1, excited by ICE and matched using a double $\lambda/4$ transmission lines at $f = 161$ MHz.

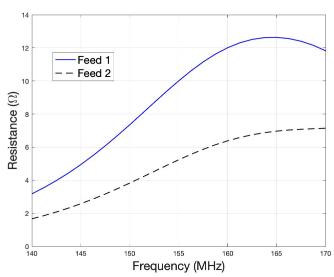

Figure 5.45: Resistance of mode 2 with ICE feeds.

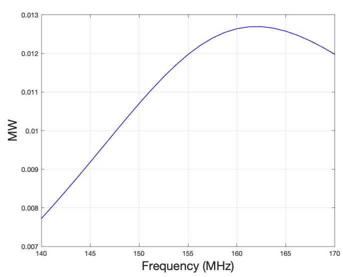

Figure 5.46: MW coefficient of mode 2 with ICE feeds.

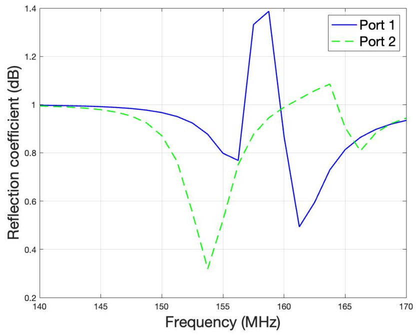

Figure 5.47: Reflection coefficient of mode 2 with a LC-matching network. Current flows between the ports over the drone body.

Material	C	D
ϵ_r	150	170
σ (S/m)	17	37

Table 5.2: Approximated carbon fiber properties to model exciting mode 1 and 2. Material C and D are both carbon fiber-reinforced polymer but depending on the direction of the carbon fibers relative to the incident electric field the conductivity, σ and relative permittivity, ϵ_r varies.

the figure exceeds 1, and this result is most likely due to the matching of each feed not being identical. This can cause currents to flow between the feeds over the drone body instead of being confined to the CM mode current. Although it is likely possible to iterate and achieve identical matching for the two feeds, implementing such a sensitive system on a drone, often operating in harsh environments, is not practical. Therefore, mode 2 is not further analyzed.

5.4.3 Exciting modes assuming carbon fiber drone

The feed of the ICE will be highly dependent on what material is used for the drone and will especially depend on the conductivity σ. Therefore, two new extreme cases were approximated based on the same measurements as the previous approximation in [29], and the two cases used are summarized in Table 5.2. The ICEs were constructed and fed the same way as the PEC case, with the wires slightly shortened. A capacitor was added in series with the source to have zero reactance around 160 MHz, and the resulting resistance is plotted in Figure 5.48.

Given that the resistance was high for all frequencies, the radiation efficiency was plotted and is presented in Figure 5.49 for the two extreme cases of the material. The radiation efficiency is low, and therefore most of the powered delivered through the wires is dissipated as heat in the drone material.

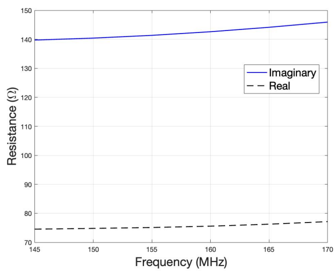

Figure 5.48: Resistance of mode 1 with ICE feeds with the drone modeled with two carbon fiber extreme material characteristics.

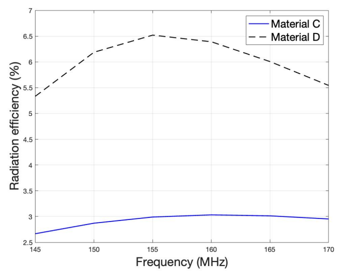

Figure 5.49: Radiation efficiency of mode 1 with ICE feeds with the drone modeled with two carbon fiber extreme material characteristics.

Chapter 6

Discussion

The goal of the project was to design an antenna that was well integrated with both the drone and the radar system while also meeting the requirements of a potential radar system. Only one of the three antennas analyzed advanced to the final step of the analysis.

The monopole antenna was highly influenced by the ground plane and the presence of drone legs. For a single dipole this could be solved by adding a symmetric ground plane, as well as moving the components further down from the drone body. However, placing two monopoles (as required by the radar system) on the same ground plane resulted in several main beams. Since the radiation of the monopole is based on the image current in the ground plane, the interactions between the elements are not surprising in hindsight. Due to the size restriction of the drone simpler solutions as increasing the size of the ground plane are ruled out.

The analysis of the CM antenna off the drone started of promising when the CM mode currents of the lowest-order modes were positioned in such a way that exciting the modes using ICE feeds would be straightforward. The first mode introduced matching challenges but could be solved relatively easily using matching networks. However, the excitement of the second mode introduced challenges that made the antenna unsuitable for the conditions in which it would operate, such as a dynamic environment with movement and varying weather. In addition, modeling the drone in carbon fiber resulted in higher resistance, and most of the power delivered was dissipated in the drone material rather than being radiated.

Although there may be a solution to get the monopole and CM antennas to work, the challenges encountered suggest that there are better alternatives available. The effort required may not be worth it, making other solutions more practical. However, the dipole antenna proved robust and was implemented on the drone with challenges all within reach to solve, and the comparison of different versions will be summarized in the following section.

6.1 Comparative Analysis

The half-wavelength dipole antenna proved efficient and robust, performing well in various positions around the drone. When placed above a ground plane, the dipole radiation deviated from its characteristic omnidirectional pattern, instead

Placement	1	1	2	3	4
Beam direction	Down	Down	Down	Side	Side
Parasitic element	No	Yes	Yes	Yes	Yes
f_{center} (GHz)	1.04	1.02	1.05	1.05	1.08
BW (MHz)	104	170	147	171	140
HPBW	132° x 76°	132° x 76°	127° x 57°	135° x 77°	120° x 68°
Gain_{max}	6.1	6.4	5.8	4.2	4.3
$S_{12,\text{max}}$ (dB)	-17.8	-18.6	-23.8	-16.8	-16.9
Added ground plane	No	No	No	Yes	Yes
$\text{Weight}_{\text{max}}$ (g)	260	280	280	330	410

Table 6.1: Performance of the different versions of the dipole summarized. The different numbering of placement is defined in Section 6.1.

following the radiation in presence of a ground plane. Both beamwidth and radiation resistance were affected by the distance the dipole was placed from the drone. However, this effect can be advantageous, as it allows for simple adjustments when properly accounted for.

Using a coaxial feed requires addressing the common mode currents generated, but there is a range of commercially sold solutions. Signal leakage between R_x and T_x, can be minimized by separating the antennas or aligning them along their lengths. However, the measures are constrained by the finite spatial extent of the drone. As such, a pulsed radar application is implied.

Finally, the simulations showed that the mounting arrangement had minimal impact. The following dipole antenna positions were simulated:

1. Under the drone with R_x and T_x placed parallel along their vertical orientation.
2. Under the drone with R_x and T_x placed parallel along their lengths.
3. In front of the drone with R_x and T_x placed parallel along their lengths.
4. Under at the front of the drone with R_x and T_x placed parallel along their lengths.

For the different positions, the results are summarized in Table 6.1. The maximal weights of the antenna are based on the following rough overestimated approximation of the included components as follows:

Coaxial cable	50 g
Dipole and parasitic element	10 g
Balun	30 g
Plastic cylinder for mounting	40 g
Chicken wire ground plane	50 g

The weight of the radar system with the dipole antenna will therefore range at most between 510-660 g (including the SDR weight).

The beamwidth allows for the formation of a common wavefront. Depending on the beam directions, either of the two common wavefront radar phased arrays shown in Figures 3.4 and 3.5 is suitable. Referring to the system analysis in Chapter 3, particularly the detection range, adjusting the gain to 4 dB with operating frequency at 1 GHz enables a detection range exceeding 600 meters with five elements and slightly over 1000 meters with ten elements. Since the drone will not operate at such high altitudes, it is preferred to use the range potential scanning from the side. Although this configuration slightly increases the weight due to the inclusion of a chicken wire ground plane, the total system weight remains well below the 1 kg limit.

The phased array can dynamically rearrange the number of elements in each subarray to adjust beam directivity and signal strength based on feedback. Increasing the bandwidth of the antenna would improve the resolution of the range, a most commonly desirable property. However, this would require managing the synthetically increased bandwidth of the SDR and integrating the parasitic element. The added weight of the parasitic element is negligible, especially when using placement 3, where the mounting components are small. This setup is particularly advantageous for imaging applications, as it enables the radar system to scan the scene from the side. Increasing the bandwidth improves the image resolution in one direction. Furthermore, the added weight has a minimal effect on hovering time, allowing the same cross-range resolution to be achieved with or without increased bandwidth.

When a large signal strength is required, or when radiation sideways is blocked, such as over cities with skyscrapers, radiating straight downward, or at a slight angle using the distributed phased array can be advantageous. Although the configuration does not allow for the determination of velocity along the same plane as the ground of the target, range and velocity measurement perpendicular to the ground are feasible. If transmitted power of the signal is large, the potential of penetrating mediums is worth considering. However, many such applications operate at lower frequencies with wider bandwidths than the purposed designs.

6.2 Future Work

For a distributed phased array with a common wavefront, the sleeve dipole shows potential for use on drones. This antenna, with an omnidirectional radiation pattern, is widely recognized since it is used on WiFi routers. The commercial use of the antenna results in limited published guidelines on its design principles. As a result, optimal performance was not achieved within the project timeframe.

Printed antennas, made with lightweight dielectric materials, also offer a potentially promising option. For example, a printed Vivaldi antenna could potentially offer a wider bandwidth.

Furthermore, implementing a more advanced distributed phased array on drones, where the beams add constructively at the target, requires precise beam steering at each element. Addressing this functionality would necessitate the development of a more directive antenna tailored for this purpose.

Chapter 7

Conclusion

In this project, potential radar distributed phased array systems implemented using drones were analyzed and antenna designs suggested based on potential radar systems. The radar system analysis essentially identified three categorizations of the array; two of which assuming that a common wave front is formed, either radiating downward or towards the side, and one where the constructive interference forms at the target position. The antenna design was aiming to suit the common wavefront case, and three antennas, a half-wavelength dipole antenna, a monopole antenna and a CM antenna, all with potential desired properties, were further investigated in the presence of the drone. Of the three suggestions, only the half-wavelength dipole antenna was seamlessly integrated on the drone while maintaining a useful radiation pattern, desired matching properties, and being lightweight to enable the drone to hover as long as possible. In addition, to increase the bandwidth, a parasitic element was added and the bandwidth was successfully increased 63 % without significant effect on the radiation pattern. Furthermore, the dipole proved itself robust and adaptable, as the radiation direction could be manipulated by placing the radiating and parasitic elements in different positions around the drone, and by considerately adding an additional ground plane, having the dipole antenna design suitable for different applications.

References

[1] Hannah Ritchie, Pablo Rosado, and Max Roser. *Data Page: Number of recorded natural disaster events*. Part of the publication: "Natural Disasters". Data adapted from EM-DAT, CRED / UCLouvain. 2022. URL: https://ourworldindata.org/grapher/number-of-natural-disaster-events.

[2] Armed Conflict Location Event Data Project (ACLED). *ACLED Website*. Data retrieved from ACLED's official website. 2025. URL: https://acleddata.com.

[3] Berk Cetinsaya, Dirk Reiners, and Carolina Cruz-Neira. "From PID to swarms: A decade of advancements in drone control and path planning - A systematic review (2013–2023)". In: *Swarm and Evolutionary Computation* 89 (2024), p. 101626. ISSN: 2210-6502. DOI: https://doi.org/10.1016/j.swevo.2024.101626. URL: https://www.sciencedirect.com/science/article/pii/S2210650224001640.

[4] Stephan Dill et al. "A drone carried multichannel Synthetic Aperture Radar for advanced buried object detection". In: *2019 IEEE Radar Conference (RadarConf)*. 2019, pp. 1–6. DOI: 10.1109/RADAR.2019.8835814.

[5] Aldi Rivaldi Dwinanda et al. "Effects of Drone Height Fluctuations on Detection of Respiratory Vital Signs Using FMCW Radar". In: *2023 IEEE International Symposium On Antennas And Propagation (ISAP)*. 2023, pp. 1–2. DOI: 10.1109/ISAP57493.2023.10388930.

[6] Chathura Wanniarachchi, Prasad Wimalaratne, and Kasun Karunanayaka. "Formation Control Algorithms for Drone Swarms and The Single Point of Failure Crisis: A Review". In: *2024 IEEE 33rd International Symposium on Industrial Electronics (ISIE)*. 2024, pp. 1–6. DOI: 10.1109/ISIE54533.2024.10595819.

[7] Jason M Merlo, Serge R Mghabghab, and Jeffrey A Nanzer. "Wireless picosecond time synchronization for distributed antenna arrays". In: *IEEE Transactions on Microwave Theory and Techniques* 71.4 (2022), pp. 1720–1731.

[8] Russell H Kenney, Justin G Metcalf, and Jay W McDaniel. "Wireless Distributed Frequency and Phase Synchronization for Mobile Platforms in Cooperative Digital Radar Networks". In: *IEEE Transactions on Radar Systems* 2 (2024), pp. 268–287.

[9] Stuart William Harmer and Gianluca De Novi. "Distributed Antenna in Drone Swarms: A Feasibility Study". In: *Drones* 7.2 (2023). ISSN: 2504-446X. DOI: 10.3390/drones7020126. URL: https://www.mdpi.com/2504-446X/7/2/126.

[10] David J Griffiths. *Introduction to electrodynamics*. Cambridge University Press, 2017.

[11] Mark A. Richards, James A. Scheer, and William A. Holm, eds. *Principles of Modern Radar: Volume 1–Basic Principles*. Raleigh, NC: SciTech Publishing, Inc., 2010. ISBN: 978-1891121524.

[12] Constantine A Balanis. *Antenna theory: analysis and design*. John wiley & sons, 2005.

[13] Sophocles J. Orfanidis. *Electromagnetic Waves and Antennas*. Available online: https://www.ece.rutgers.edu/~orfanidi/ewa/. New Brunswick, NJ: Rutgers University, 2016.

[14] Gary Breed. "Improving the bandwidth of simple matching networks". In: *High Frequency Electron* 7.56-60 (2008).

[15] Daniel Sjöberg and Mats Gustafsson. *Kretsteori, ellära och elektronik*. svenska. Elektro- och informationsteknik, 2021.

[16] B Steinberg. "The peak sidelobe of the phased array having randomly located elements". In: *IEEE Transactions on Antennas and Propagation* 20.2 (1972), pp. 129–136.

[17] M. Donvito and S. Kassam. "Characterization of the random array peak sidelobe". In: *IEEE Transactions on Antennas and Propagation* 27.3 (1979), pp. 379–385. DOI: 10.1109/TAP.1979.1142097.

[18] Y. Lo and R. Simcoe. "An experiment on antenna arrays with randomly spaced elements". In: *IEEE Transactions on Antennas and Propagation* 15.2 (1967), pp. 231–235. DOI: 10.1109/TAP.1967.1138876.

[19] Jeffrey A Nanzer et al. "Distributed phased arrays: Challenges and recent advances". In: *IEEE Transactions on Microwave Theory and Techniques* 69.11 (2021), pp. 4893–4907.

[20] Roy W Lewallen. "Baluns: What they do and how they do it". In: *The ARRL Antenna Compendium* 1 (1985), pp. 157–164.

[21] Bashar Bahaa Qas Elias et al. "A review of antenna analysis using characteristic modes". In: *IEEE Access* 9 (2021), pp. 98833–98862.

[22] Ting-Yen Shih and Nader Behdad. "Bandwidth enhancement of platform-mounted HF antennas using the characteristic mode theory". In: *IEEE transactions on antennas and propagation* 64.7 (2016), pp. 2648–2659.

[23] Francesco Alessio Dicandia and Simone Genovesi. "A compact CubeSat antenna with beamsteering capability and polarization agility: Characteristic modes theory for breakthrough antenna design". In: *IEEE Antennas and Propagation Magazine* 62.4 (2020), pp. 82–93.

[24] R Tanner. "Shunt and notch-fed HF aircraft antennas". In: *IRE Transactions on Antennas and Propagation* 6.1 (1958), pp. 35–43.

[25] Robert Martens, Eugen Safin, and Dirk Manteuffel. "Inductive and capacitive excitation of the characteristic modes of small terminals". In: *2011 Loughborough Antennas & Propagation Conference*. IEEE. 2011, pp. 1–4.

[26] Rafik Zitouni, Laurent George, and Stefan Ataman. "Software-defined radio for wireless mesh networks". In: June 2022, pp. 81–103. ISBN: 9781839532825. DOI: 10.1049/PBTE101E_ch5.

[27] International Telecommunication Union. *Attenuation in vegetation.* Recommendation ITU-R P.833-9. Available: https://www.itu.int/rec/R-REC-P.833-9-201609-I. 2016.

[28] Samuel Prager et al. "Snow depth retrieval with an autonomous UAV-mounted software-defined radar". In: *IEEE Transactions on Geoscience and Remote Sensing* 60 (2021), pp. 1–16.

[29] Zhen Li et al. "X-band microwave characterisation and analysis of carbon fibre-reinforced polymer composites". In: *Composite Structures* 208 (2019), pp. 224–232.